WIND ENERGY
Wind Energ. 2009; **12**:1–32
Published online 19 June 2008 in Wiley Interscience
(www.interscience.wiley.com) DOI: 10.1002/we.280

Estimating the Angle of Attack from Blade Pressure Measurements on the National Renewable Energy Laboratory Phase VI Rotor Using a Free Wake Vortex Model: Yawed Conditions

Tonio Sant*, Mechanical Engineering Department, Faculty of Engineering, University of Malta, Msida, Malta, MSD 07
Gijs van Kuik and G. J. W. van Bussel, Section Wind Energy, Faculty of Aerospace Engineering, Delft University of Technology, Kluyverweg 1, 2629 HS, Delft, The Netherlands

Key words: wind turbine; yawed conditions; blade element momentum theory; National Renewable Energy Laboratory phase VI experiments; free wake vortex model; wake vorticity; aerofoil data; dynamic stall

Wind turbine design codes for calculating blade loads are usually based on a blade element momentum (BEM) approach. Since wind turbine rotors often operate in off-design conditions, such as yawed flow, several engineering methods have been developed to take into account such conditions. An essential feature of a BEM code is the coupling of local blade element loads with an external (induced) velocity field determined with momentum theory through the angle of attack. Local blade loads follow directly from blade pressure measurements as performed in the National Renewable Energy Laboratory (NREL) phase IV campaign, but corresponding angles of attack cannot (on principle) be measured. By developing a free wake vortex method using measured local blade loads, time-dependent angle of attack and induced velocity distributions are reconstructed. In a previous paper, a method was described for deriving such distributions in conjunction with blade pressure measurements for the NREL phase VI wind turbine in axial (non-yawed) conditions. In this paper, the same method is applied to investigate yawed conditions on the same turbine. The study considered different operating conditions in yaw in both attached and separated flows over the blades. The derived free wake geometry solutions are used to determine induced velocity distributions at the rotor blade. These are then used to determine the local (azimuth time dependent) angle of attack, as well as the corresponding lift and drag for each blade section. The derived results are helpful to develop better engineering models for wind turbine design codes. Copyright © 2008 John Wiley & Sons, Ltd.

Received 11 April 2006; Revised 4 February 2008; Accepted 2 May 2008

* Correspondence to: T. Sant, Section of Wind Energy, Faculty of Aerospace Engineering, Delft University of Technology, Kluyverweg 1, 2629 HS, Delft, The Netherlands.
E-mail: tonio.sant@um.edu.mt

Introduction

In the real operating environment of a horizontal-axis wind turbine, the direction of the wind changes frequently with respect to the rotor axis. As a result, the turbine may operate in yaw for considerable amounts of time. The yawed condition introduces a cyclic angle of attack at the blades and causes the helical wake behind the rotor to become skewed, yielding a time-dependent and a complex induced velocity distribution at the rotor plane. When the unsteady angle of attack at a blade section exceeds the aerofoil's stalling angle and the reduced frequency is high enough, dynamic stall phenomena cause the time-varying aerodynamic loads to be much higher than those predicted by two-dimensional (2-D) static aerofoil data. The hysterisis effects introduced by dynamic stall may have a negative effect on the aeroelastic damping behaviour of wind turbine blades. This reduces the fatigue lifetime leaving an adverse impact on the economics of the system.

The blade element momentum (BEM) theory is still the most commonly used method for computing aerodynamic loads during the aeroelastic design of wind turbine blades. Although this theory is suitably accurate for modelling axial conditions provided that reliable aerofoil data are used, it is unreliable when treating unsteady conditions associated with yaw. In the past years, several engineering models were added to BEM codes to improve their accuracy in predicting the aerodynamic loads for yawed wind turbine rotors. These models fall under two classifications:

- Type I models are those that correct the standard 2-D aerofoil data for three-dimensional (3-D) effects (stall delay) and unsteady aerodynamic effects (unsteady aerofoil models for both attached flow and dynamic stall). Examples of models used to correct for 3-D effects are described.[1–3] Examples for unsteady aerofoil models used in attached flow conditions are Theodorsen's model[4] and Leishman's indicial response method using Duhamel's superimposition.[5] Examples of dynamic stall models include the ONERA model, Boeing-Vertol model and the Beddoes–Leishman model. A description of these models may be found in Leishman.[5,6] Most unsteady aerofoil models for attached flow conditions are based on 2-D non-rotating wings, and therefore they may be inaccurate when applied for 3-D conditions on a rotating wind turbine blade. Consequently, they are also inaccurate when treating 3-D dynamic stall on a rotating blade. Because of yawed flow operation, each rotating blade is subjected to unsteady radial flow components that may be much larger in magnitude than in a non-yawed rotor. Such radial flows influence the dynamic stall behaviour significantly, as described.[7] Although it is a well-known fact that radial flow over the blades helps in preventing flow separation over the blades at high angles of attack and thus contributes to stall delay, it is still unclear how 3-D effects influence stall in an unsteady environment.
- Type II models are those that correct the axial induction factor computed by the BEM theory for the uneven axial induced velocity distribution at the rotor plane resulting from the skewed wake. An early model for skewed wake effects has been proposed by Glauert[8] has the form

$$a_c = a\left[1 + K\frac{r}{R}\sin(\phi)\right] \tag{1}$$

  where K is a parameter that depends on the yaw angle. Detailed inflow measurements on the Delft wind tunnel model rotor and computations using the more advanced free wake vortex model revealed that this model is inaccurate because it only considers the induction from the trailing blade tip vorticity and ignores that contributed by the root vorticity.[9,10] Other models were developed in the past years, e.g. in the JOULE Dynamic Inflow projects[11,12], and have been implemented in various BEM-based aeroelastic models. Although these models improved load predictions, considerable improvement is still required. This was noted during the 'blind comparison' investigation organized by the National Renewable Energy Laboratory (NREL) in the year 2000.[13,14] Significant discrepancies between predicted and experimental results were observed even at low wind speeds at which the angle of attack is small.

Detailed surface pressure measurements on a rotating blade of a yawed wind turbine rotor are very useful in obtaining a deeper understanding of yaw aerodynamics. Such measurements were taken in 2000 on the NREL phase VI rotor when tested in the NASA Ames 80 × 120 ft wind tunnel. The pressures were integrated

DOI: 10.1002/we

along the blades to yield the local blade normal and tangential aerodynamic loads. These data have been analysed by various researchers and used for bases of comparison with state-of-the-art aerodynamic codes modelling both axial[15–21] and yawed conditions.[20–23] A major difficulty with analyzing experimental measurements is to determine the angle of attack at the different blade sections. When treating steady 2-D flows, the concept of angle of attack is well defined and easily understood. However, defining the angle of attack for a rotating blade in which the flow becomes highly 3-D and complex is ambiguous. The concept of angle of attack is even more difficult to define in yawed rotors where the flow becomes unsteady. Unlike more advanced models such as those based on vortex panel methods and CFD, BEM-based aerodynamic models reduce the complex 3-D flow around the blades to a simplified 2-D strip. For this reason, BEM-based aerodynamic models indispensably require a definition of the angle of attack to be able to compute the local loads from the calculated induction and blade relative flow velocities. The angle of attack in BEM theory is usually defined as follows

$$\alpha = \tan^{-1}\left(V_n / V_t\right) \tag{2}$$

where V_n and V_t are the local normal and tangential flow components, respectively, as indicated in Figure 1.

V_n and V_t are obtained by momentum theory considerations, usually corrected with some (semi-empirical) factors for finite number of blades, high axial trust coefficients, yaw, etc.

In a previous paper,[24] a method was presented for using a free wake vortex model to derive the angle of attack from the measured C_n and C_t values of the NREL rotor in axial conditions. In that approach, an angle of attack distribution is initially assumed at the blades. This angle is used to determine C_l from the measured C_n and C_t. An estimate for the bound circulation at the blades is then made using the Kutta–Joukowski law. This bound circulation is then prescribed to the free wake vortex model to generate a free wake, from which the induction at the blades and a new angle of attack are then obtained. This process is repeated until convergence in the angle of attack is achieved.

The objective of this paper was to apply the same method for finding the angle of attack for yawed conditions. A free wake vortex model is adequate to model the complex skewed wake geometry of a yawed wind turbine since the model wake is allowed to develop freely under the action of the wake induced velocities. In a lifting line, free wake model problems arise when calculating the induced velocities at the lifting line itself. Vorticity shed from the lifting line induces a (logarithmic) singularity at that location. A way to come around this is either the introduction of a higher-order lifting line approach or the use of an unsteady panel method. In the present implementation of the free wake model, shed and trailing vorticity are assumed to be generated at the trailing edge of the rotor blade (see Figure 2). This is equivalent to assuming a panelled distribution of

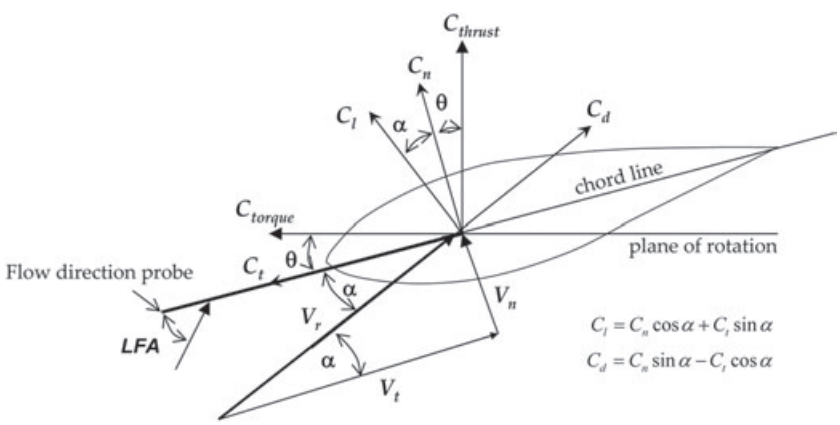

Figure 1. Blade section aerodynamic load coefficients

DOI: 10.1002/we

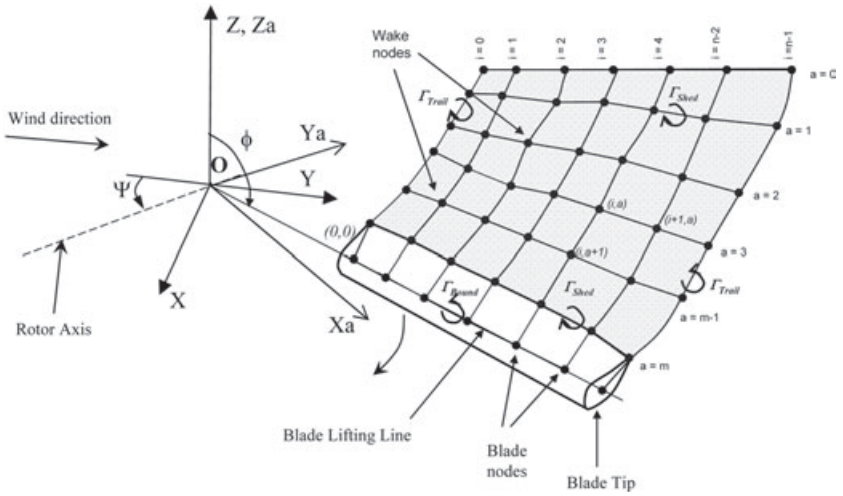

Figure 2. Modelling of the near wake

vorticity over the rotor blade itself. Thus, non-singular induced velocities are obtained at the bound vortex line, which is assumed to be located at the 0.25 chord position. More details can be found in the section below describing the methodology.

The unsteady angle of attack distributions are derived for different operating conditions in yaw of the NREL rotor. These are then used to obtain the aerofoil data for both unsteady attached flow and dynamic stall conditions. These aerofoil data are then compared with data obtained for axial conditions as well as with the 2-D wind tunnel data for the same aerofoil. From the free wake plots, the time-dependent induced velocity distributions at the rotor plane are computed and analysed. The free wake vortex calculations provide further insight on how the bound circulation at the blades is convected into the wake in the form of trailing and shed vorticity, and how these influence the induction at the blades. Using the derived aerofoil data and induced velocity distributions, the rotor aerodynamic loads can be calculated and compared with those measured at the wind tunnel experiments. The results of this study provide further insight on how to improve BEM-based aerodynamic models in aeroelastic design codes for modelling wind turbines in yawed conditions. Both the derived aerofoil data and induced velocity distributions can be helpful in improving such models.

NASA/Ames Unsteady Aerodynamics Experiment (UAE) Wind Tunnel Data Used

The NASA phase VI rotor is a two-bladed 10 m diameter wind turbine rotor. The geometry of the blades is based on the S809 aerofoil. Details about the blade design may be found in Giguere and Selig.[25] One of the blades was equipped with pressure sensors at five radial locations: 0.30R, 0.47R, 0.63R, 0.80R and 0.95R to measure the surface pressures. The blade was also equipped with five-hole pressure probes at 0.34R, 0.51R, 0.67R, 0.84R and 0.91R to measure the local flow angle (LFA) (Figure 1). At each of these radial locations, the surface pressures were integrated to obtain C_n, C_t and C_m. Strain gauge techniques were used to measure the low-speed shaft torque and the blade root flap and edge moments at one of the blades. Further information about these UAE experiments is available.[13,26] The turbine was tested over a wide range of operating conditions. This study only considered yawed conditions with the rotor operated in the upwind configuration. The cases are shown in Table I. Yaw angles beyond 30º were not included in this study since their measurements were expected to be considerably affected by the flow disturbances from the box/boom installed upstream of the rotor.[26] The blade pitch and rotor coning angle were maintained constant at 3º and 0º, respectively.

DOI: 10.1002/we

Table I. Operational conditions considered in the present study

Data file	Air density (kg m^{-3})	Wind speed (m s^{-1})	Rotational speed (rpm)	Tip speed ratio $\left(\frac{R\Omega}{U}\right)$	Measured rotor thrust coefficient $\left(\frac{T}{\frac{1}{2}\rho A U^2}\right)$	Measured rotor power coefficient $\left(\frac{P}{\frac{1}{2}\rho A U^3}\right)$
S0500300	1.244	5.0	71.7	7.58	0.43	0.23
S1000300	1.246	10.1	72.0	3.81	0.29	0.17
S1500300	1.225	15.1	72.2	2.53	0.19	0.07

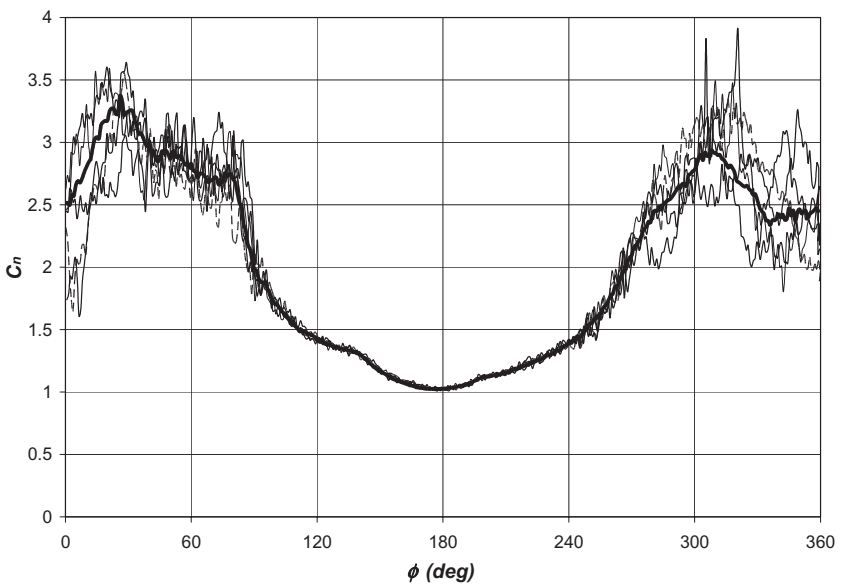

Figure 3. Variation of the normal force coefficient with blade azimuth angle for 30º yaw, U = *15 m s^{-1} and* r/R = *0.3. Values for five separate cycles are shown, and the cycle mean is indicated by the bold curve*

For each operating condition, data records of the surface pressures were taken for 36 individual rotor rotations (cycles). Figure 3 shows the typical variations for C_n obtained at each individual cycle at 0.3R at 30º yaw and a wind speed of 15 m s^{-1}. In this figure, data from five different cycles are shown. It may be observed that for blade azimuth angles between approximately 120º and 240º, the cycle-to-cycle variation is very small. For this region of blade azimuth angle, the angle of attack is small and the flow is attached. For the other blade azimuth angles, the cycle-to-cycle variation is large, and this is because of the high angles of attack where flow separation influences reduce the repeatability of the measured data. In all cases, the mean (indicated by the solid black line in Figure 3) is considered for the analysis with the free wake code.

Free Wake Vortex Model

The free wake vortex model was specifically designed to simulate rotor wakes based upon knowledge of the aerodynamic loads at the blades. Only a brief outline of the model is given here, but a detailed description is presented in Sant *et al*.[24] Unlike other free wake vortex models, it does not directly rely on the availability of aerofoil data to iteratively determine the blade loads. The bound circulation distribution is prescribed as input.

DOI: 10.1002/we

From this prescription, the code generates a free wake and then calculates the 3-D induced velocities at different points in the flow field of the rotor. In the model, the blades are represented by lifting lines at the quarter chord locations and are discritized using a cosine segmentation. The near wake consists of vortex sheets, one per blade, with trailing and shed vorticity assumed to originate from the trailing edges of each blade. The vortex sheets are modelled as a mesh of straight line vortex filaments, interconnected by wake nodes to represent trailing and shed vorticity as shown in Figure 2. The wake nodes leave the blades from the trailing edges, from which they advance after each time step downstream with a local velocity that is equal to the vectorial sum of the free stream velocity and the vorticity-induced velocity computed from the Biot–Savart equation.

Viscous effects are catered for in the near wake by applying the approach described by Leishman *et al*.[27] for modelling core growth of a rolled-up tip vortex. However, in this paper, the core growth model is applied to each shed and trailing vortex filament. In this viscous modelling, two parameters need to be prescribed[24]: δ_v which is the turbulent viscous coefficient, and S_c which is a time-offset parameter that defines the size of the viscous cores of the filaments at the point of their origin (i.e. at the trailing edge of the rotor blades). The effect of filament stretching is also included in this model. It is realized by the authors that the adopted viscous core model was not developed to represent the actual growth in thickness of the boundary layer shed by the rotor blades in the wake. However, by choosing the parameters δ_v and S_c such that the resulting viscous core size is in the same range as the expected trailing edge thickness of the boundary layer, a stable computational model optimized with regard to time demand is obtained. In the previous paper,[24] treating the axial (non-yawed) cases, the tuning of these parameters is discussed in more detail.

The far wake model consists of a helical tip vortex at each blade, representing the fully rolled-up tip vortices. Each helical tip vortex is attached to the outboard end of the corresponding near wake. It is assumed that, at the transfer of the near-to-the-far wake model, each near wake vortex sheet rolls up immediately into a concentrated tip vortex. This assumption is not physical, but was found to yield accurate predictions for the inflow at the rotor plane and near wake geometry in a validation study performed on the subject free wake vortex model.[28] The helices of the far wake extend downstream with prescribed pitch, number of rotations and wake skew angle. Since in a yawed rotor, the bound circulation at the blades is a function of azimuth angle, then the vorticity assigned to each far wake filament is varied, depending on its azimuth position on the helix.

Methodology

Procedure

The method for deriving the angle of attack from the blade pressure measurements consists of an iterative procedure which starts off by an initial assumption of the angle of attack distribution at the blades. This is used to find C_l from the measured C_n and C_t (Figure 1). The bound circulation at the blades is then estimated using the Kutta–Joukowski law at the pressure measurement locations (30, 47, 63, 80 and 95% R). A double interpolation is used to obtain a continuous bound circulation distribution at the blades as a function of radial position and blade azimuth angle ($\Gamma_B[r/R, \phi]$), with the bound circulation at the tip and root set to zero. For interpolating, a spline interpolation was initially applied to obtain a distribution of Γ_B as a function of r/R. However, it was found that the number of pressure measurement stations (five) was not sufficient to yield a smooth representation of the bound circulation distribution along the blades with a spline method because it resulted in unrealistic 'jumps'. Alternatively, a linear interpolation is adopted. Spline interpolation is only used to interpolate for different blade azimuth positions. This bound circulation distribution is then prescribed to the free wake vortex model to generate a free wake. The induced velocity distributions at the blades are then found by applying the Biot–Savart law to compute the induction at each of the blade nodes located on each lifting line, adding up all contributions of the bound vortex filaments, the trailing and shed vortex filaments of the near free wake (see Figure 2) and the filaments of the prescribed far wake. The induced velocity at each blade node is then added vectorially to the geometric velocity of the blades to determine the local normal and tangential flow velocity components, V_n and V_t (Figure 1). A new angle of attack is then found using equation

DOI: 10.1002/we

(2). This process is repeated until convergence in the angle of attack is achieved. The step-by-step procedure is described in detail in Sant *et al*., section 4.0.[24]

Selecting Free Wake Model Parameters

Initially, a parametric analysis was performed to examine the numerical behaviour of the free wake vortex model at $\Psi = 30^{\circ}$ for different values of blade and wake discretization parameters (n, $\Delta\phi$, *nRev*). The computational cost of free wake vortex models increases very rapidly as finer spatial and temporal discritization levels are used. This analysis was therefore necessary to ensure that the selected parameters yield minimal numerical errors, while maintaining the computational time within practical limits. The parametric analysis also investigated the influence of the different values of viscous core parameters (δ_v, S_c) on the induced velocity and angle of attack obtained at the blades. The following four different tests were performed:

- Test A investigated how the different values of *nRev* influence the calculated induced velocities and angle of attack at the blades. In the free wake solution, the near wake had to extend far enough downstream such that the induced velocity at the rotor plane is independent of *nRev*. To satisfy this condition, wake periodicity should be achieved such that the induced velocity at the blade lifting line between two successive revolutions should be the same, at each azimuth angle, ϕ. The discrepancy is expressed here as

$$\text{Percentage discrepancy} = \frac{u_{y,c}\big|_{\phi,nRev-1} - u_{y,c}\big|_{\phi,nRev}}{u_{y,c}\big|_{\phi,nRev}} \times 100 \tag{3}$$

  For this test, parameters n, $\Delta\phi$, δ_v and S_c were kept constant at 21, 10º, 500 and 1, respectively, while only *nRev* was varied, using successive values of 1, 2, 3, 4 and 5. To obtain the suitable wake periodicity while maintaining reasonable computational costs, *nRev* had to be selected according to the wind speed. *nRev* was taken to be equal to 5, 4 and 3 at wind speeds $U = 5$, 10 and 15 m s^{-1}, respectively. The near wake extended downstream by *1.8d*, *3d* and *3.5d*, respectively. At these distances, the values for the percentage discrepancy in the induced velocity at the blades ($u_{y,c}$) was <1.5% at radial locations $0.29 < r/R < 0.96$. The corresponding percentage discrepancy in the angles of attack computed at the blades was <0.08% for the same radial locations. At these selected values of *nRev*, the far wake was enough downstream such that its contribution to the induction at the rotor plane was very small (<3% of the total induction).

- Test B investigated the sensitivity of the induced velocity and the angle of attack distributions at the blades to different azimuthal step sizes ($\Delta\phi$). This test was carried out at $U = 13$ m s^{-1} by varying $\Delta\phi$ while keeping all other parameters fixed. Four values of $\Delta\phi$ were chosen, equal to 7.5º, 10º, 15º and 30º, while n, *nRev*, δ_v and S_c were kept constant at 31, 2, 500 and 1, respectively. Figure 4(a),(b) illustrates the spanwise variations of the computed axial induced velocity and angle of attack at the blade lifting line for azimuth angles 0º (blade vertical pointing upwards), 120º and 240º. Selecting a rotor azimuthal time step of 10º instead of 7.5º reduced the computational time required by more than half while maintaining a relative error in $u_{y,c}$ and α less than 0.06 m s^{-1} and 0.05º, respectively.
- Test C investigated the sensitivity of the distributions for the induced velocity and angle of attack at the blades to various values of n (11, 21 and 31). This test was carried out at $U = 13$ m s^{-1} and $\Delta\phi$, *nRev*, δ_v and S_c were set to 10º, 2, 500 and 1, respectively. Figure 5(a),(b) shows the spanwise variations of $u_{y,c}$ and α for blade azimuth angles 0º, 120º and 240º computed for the three different values of n. It can be noted from this figure that there is a significant change in the results when increasing n from 11 to 21, but such change is minimal when going from n being 21 to 31. Choosing n equal to 21 instead of 31 saves the computational time by approximately a half, with a relative error of less than 0.1 m s^{-1} and 0.3º in $u_{y,c}$ and α, respectively, over $0.29 < r/R < 0.96$.
- Test D studied the influence of parameters (δ_v, S_c) on $u_{y,c}$ and α. As already discussed,[24] it is very difficult to select the optimum values for (δ_v, S_c) used in the vortex model to cater for viscous effects. This is even more difficult when modelling yawed conditions in which viscous effects become subject to dynamic flow

DOI: 10.1002/we

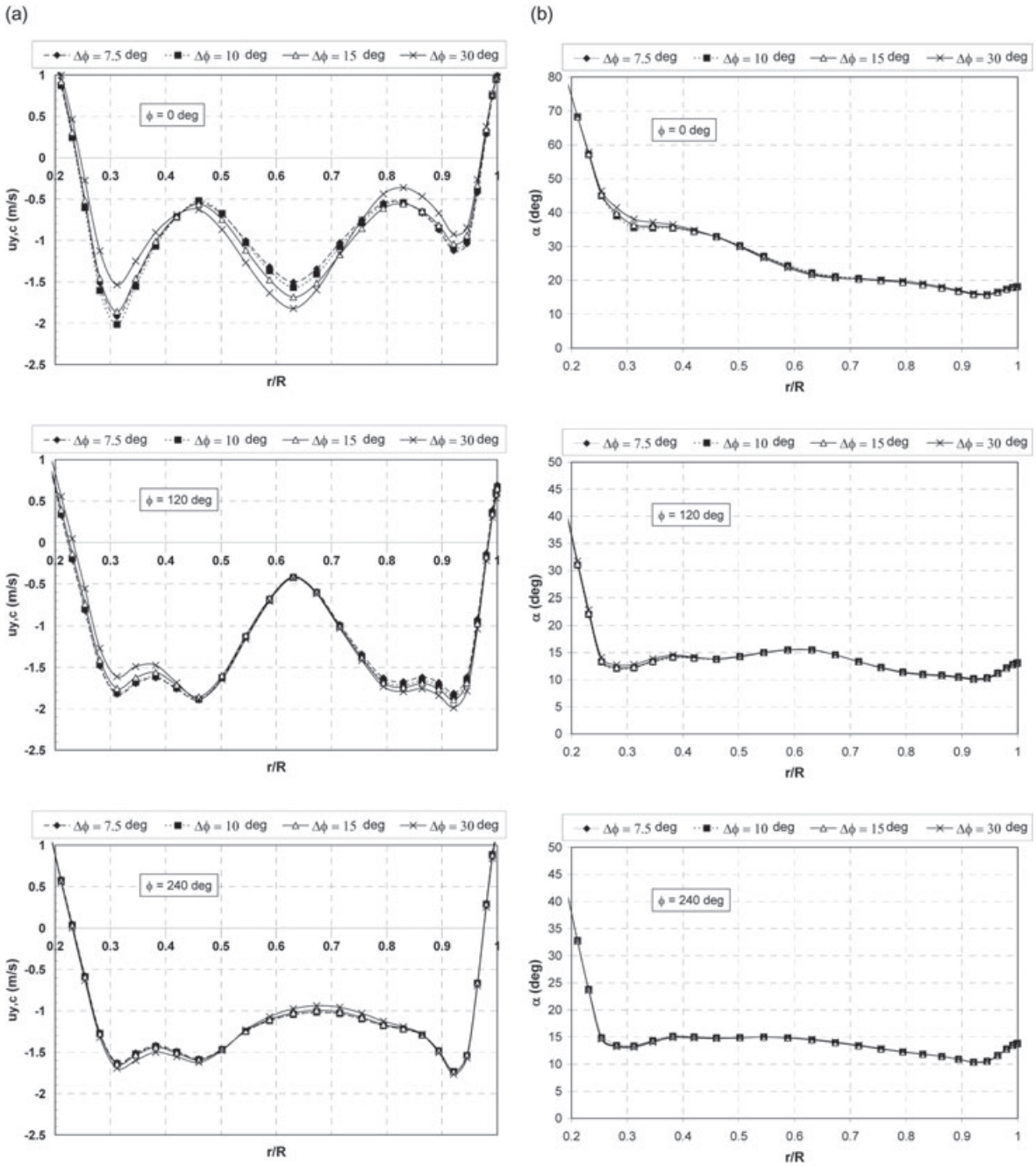

Figure 4. (a) Spanwise variation of $u_{y,c}$ *at different values of* ϕ *computed for different values of* $\Delta\phi$ *(*$\Delta\phi$ *= 7.5º, 10º, 15º, 30º);* U *= 13 m s*$^{-1}$*,* $\Psi = 30º$*; and (b) spanwise variation of* α *at different values of* ϕ *computed for different values of* $\Delta\phi$ *(*$\Delta\phi$ *= 7.5º, 10º, 15º, 30º);* U *= 13 m s*$^{-1}$*,* $\Psi = 30º$

influences. Because of this difficulty, an analysis was therefore carried out to investigate the sensitivity of $u_{y,c}$ and α to different values of (δ_v, S_c) using a similar approach as that performed in axial conditions.[24] The analysis was performed at two wind speeds only (7 and 13 m s^{-1}), which yielded attached flow and separated flow conditions at the blades, respectively. Four different sets of values of (δ_v, S_c) were used: (10, 0.1),

DOI: 10.1002/we

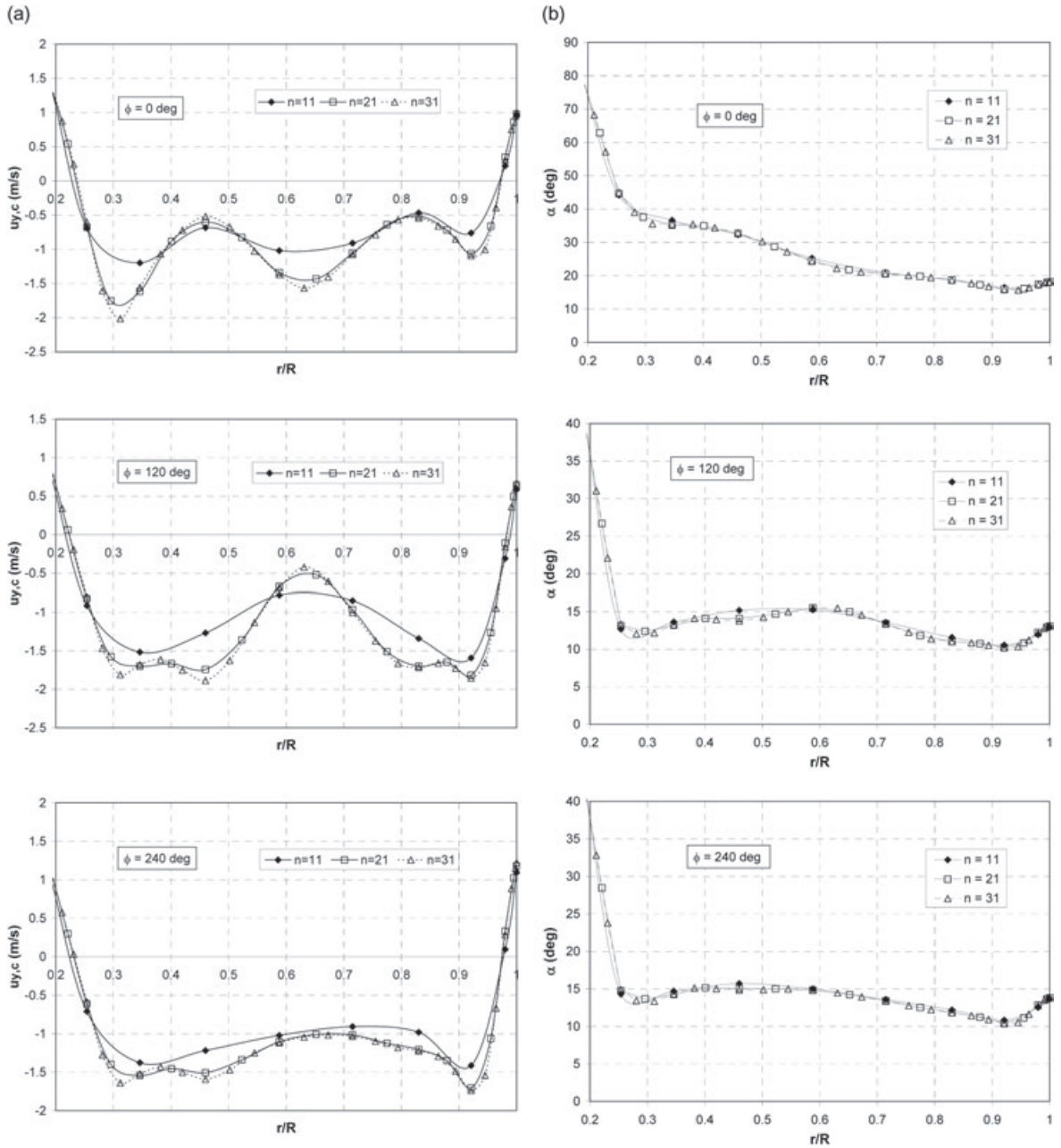

Figure 5. (a) Spanwise variation of $u_{y,c}$ *at different values of* ϕ *computed for different values of* n (n = *11, 21, 31);* U = *13 m s*$^{-1}$, $\Psi = 30^{o}$*; and (b) spanwise variation of* α *at different values of* ϕ *computed for different values of* n *(*n = *11, 21, 31);* U = *13 m s*$^{-1}$, $\Psi = 30^{o}$

(100, 1), (500, 1) and (500, 10). Figures 6 and 7 illustrate the resulting spanwise variations at different blade azimuth positions (0º, 120º and 240º). It is observed that the sensitivity of $u_{y,c}$ and α at the first three sets of values of (δ_v, S_c) is very small. But a notable relative discrepancy is seen for (500, 10). However, it was found that the latter values are too large to be realistic, and in all free wake computations (δ_v, S_c) were selected to be equal to (500, 1) as for axial conditions.

DOI: 10.1002/we

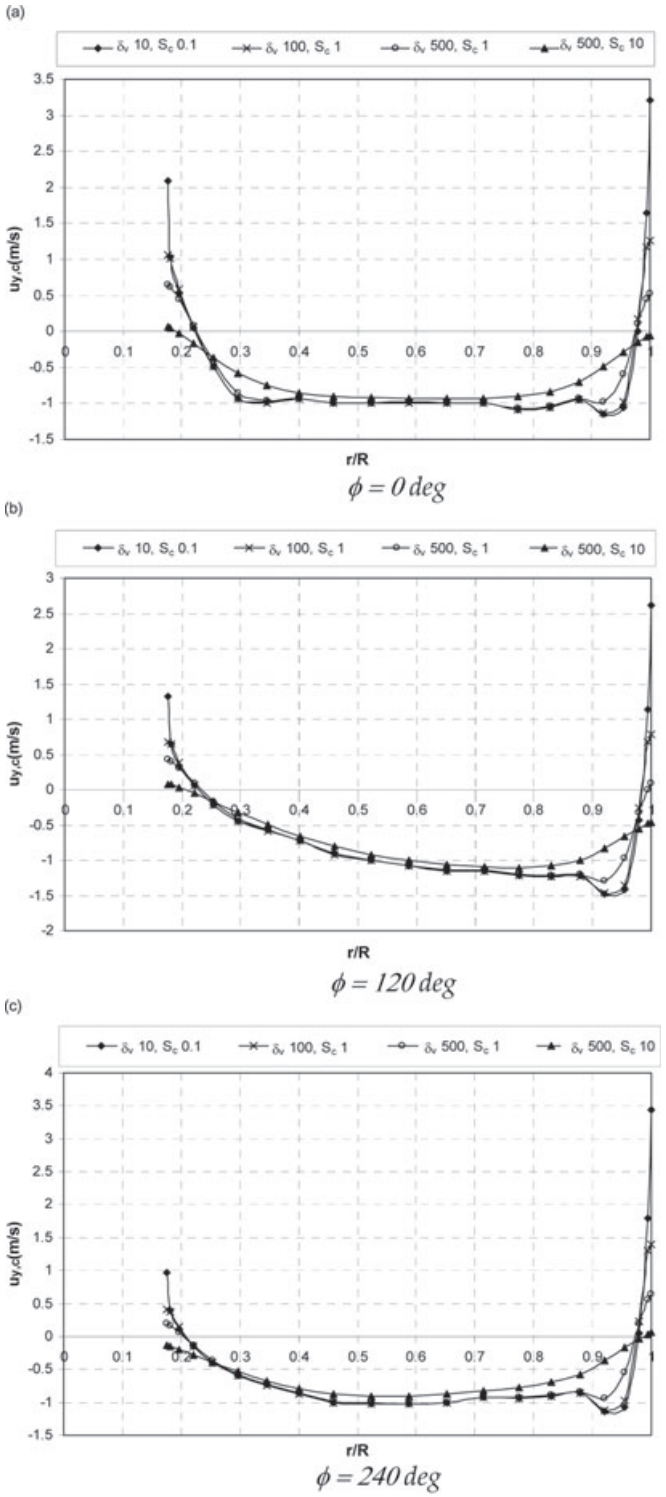

Figure 6. Effect of viscous parameters (δ_ν, S_c) *on the spanwise distribution of* $u_{y,c}$ *at different blade azimuth angles,* $U = 7\ m\ s^{-1}$

DOI: 10.1002/we

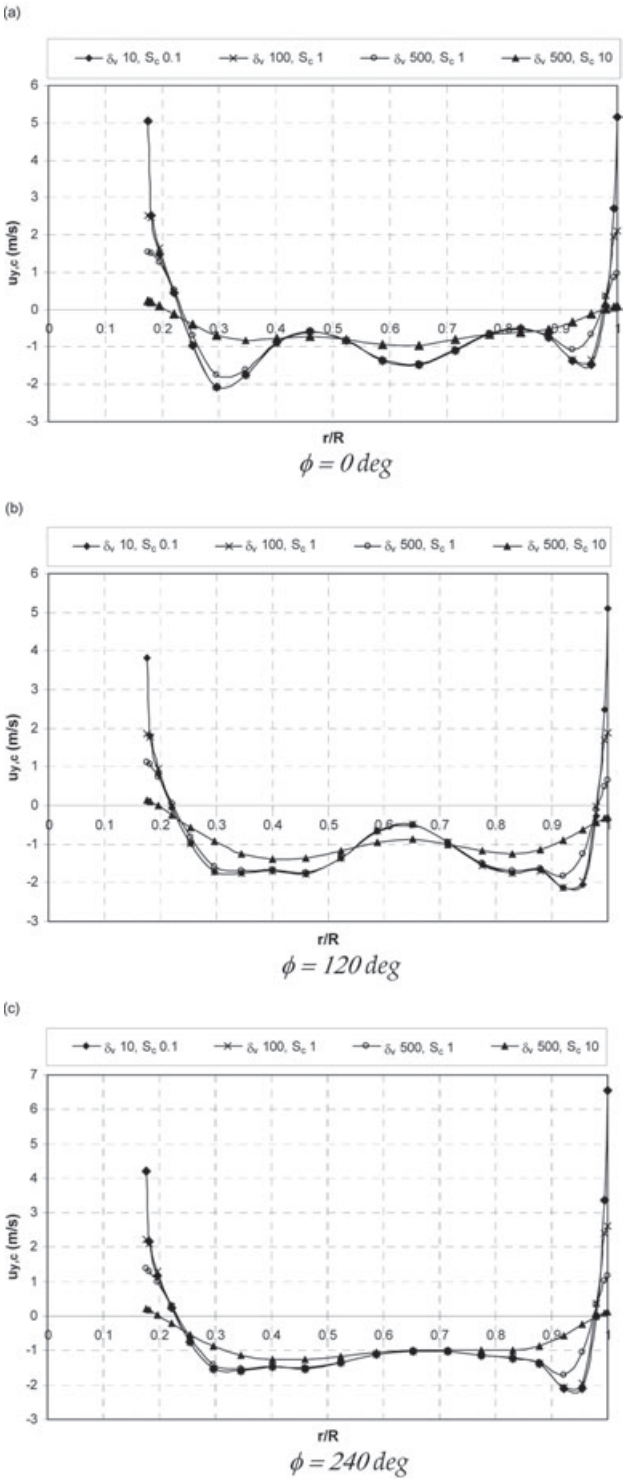

Figure 7. Effect of viscous parameters (δ_v, S_c) *on the spanwise distribution of* $u_{y,c}$ *at different blade azimuth angles,* U = *13 m s*$^{-1}$

DOI: 10.1002/we

In all the free wake computations in this paper, the azimuthal step and number of helical revolutions in the far wake were kept constant at 10º and 10, while the prescribed helical pitch and wake skew angle were varied depending on wind speed. To determine reasonable values for the prescribed helical pitch and wake skew angle at each wind speed, preliminary calculations were carried out with the same free wake model, and an estimate was obtained from the near wake geometry.

Results and Discussion

This section describes the results obtained from a converged solution in the angle of attack from the NREL blade pressure measurements at wind speeds 5, 10 and 15 m s^{-1}, and at a yaw angle of 30º using the procedure in the Methodology. Parameters n, $\Delta\phi$, δ_v and S_c were maintained constant at 21, 100, 500 and 1, respectively,while *nRev* was taken to be equal to 5, 4 and 3 at wind speeds U = 5, 10 and 15 m s^{-1}, respectively.

Variation of α, $\dot{\alpha}$, C_l and C_{dp} with Blade Azimuth Angle (ϕ)

Figure 8(a)–(c) illustrates the converged angle of attack variations together with the variations of the rate of change of the angle of attack and the lift and drag coefficients with the blade azimuth angle at each of the different tunnel wind speeds. For all wind speeds, the angle of attack varies periodically with the blade azimuth angle. At U = 5 m s^{-1}, a gradual phase shift is observed in the angle of attack when moving outboard from r/R = 0.3–0.95. At r/R = 0.3, the angle of attack is minimum at 210º, while at r/R = 0.95, the minimum occurs at 120º. For the higher wind speeds, however, (U = 10 and 15 m s^{-1}), this phase shift is not noted and the angle of attack is the minimum when the blade is approximately at the 180º position and reaches a maximum when the blade is at the 0/360º position. For a particular wind speed, both the mean and cyclic components of the angle of attack are larger at the inboard blade sections, implying that the inboard sections experience higher unsteady effects and are first to experience stall. Increasing the wind speed increases both the mean and cyclic components of the angle of attack.

In Figure 8(a)–(c), it may also be noted that the time rate of change of angle of attack ($\dot{\alpha}$) varies also periodically with blade azimuth angle at all wind speeds. The rate of change of angle of attack is negative during approximately blade angles 0º to 180º, while it is positive from about 180º to 360º. The inboard blade sections tend to experience the highest rates of change in the angle of attack, occurring at approximately blade angles 90º and 270º. Increasing the wind speed while keeping the rotor shaft speed constant results in higher values for $\dot{\alpha}$. At U = 5 m s^{-1}, $\dot{\alpha}$ at r/R = 0.3 is equal to about ±25 deg s^{-1}, while at U = 15 m s^{-1}, this reaches maximum values of about ±200 deg s^{-1}.

With regard to the variation of the lift coefficient with blade azimuth angle, it may be observed that, at each wind speed, the inboard regions of the blades experience higher values in both the mean and cyclic components of C_l. At low wind speeds (5 and 10 m s^{-1}), the variation of C_l with $\dot{\phi}$ is periodic and quite regular, reaching a maximum value at blade position 0/360º and a minimum value at about 180º. At the higher wind speeds (U = 15 m s^{-1}), the variation is no longer regular.

The pressure drag coefficients (C_{dp}) are very small at low wind speeds (U = 5 m s^{-1}). But as the wind speed is increased, the pressure drag coefficient values increase rapidly, the highest values being at the inboard blade sections at blade angles 0º–120º and 240º–360º.

Hysterisis Loops C_l-α and C_{dp}-α

From the data presented in Figure 8, it is possible to derive the unsteady aerofoil hysteresis loops for C_l-$\dot{\alpha}$ and C_{dp}-$\dot{\alpha}$. Figure 9(a)–(f) illustrates the hysteresis loops for the different wind speeds and radial locations. The 2-D steady aerofoil data obtained from the Delft low-speed, low-turbulence wind tunnel experiments are also shown. The 3-D steady aerofoil data, which were derived using the blade pressure measurements for non-yawed conditions together with the free wake code, are also included.[24] The hysteresis plots are helpful in establishing whether any particular blade section is operating in an attached or stalled flow regime. One should keep

DOI: 10.1002/we

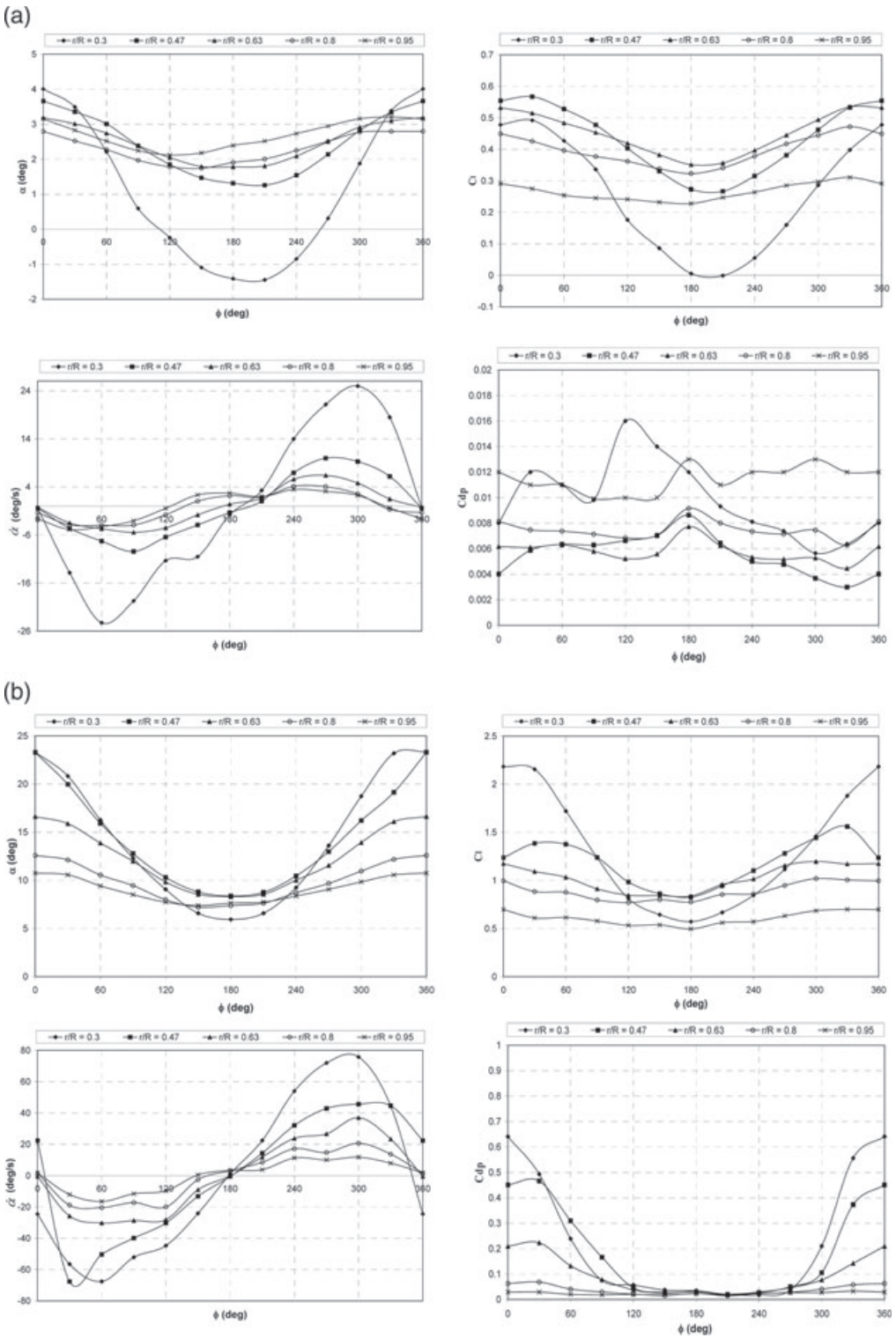

Figure 8. (a) Variation α, α, C_l *and* C_{dp} *with blade azimuth angle* (ϕ) *at* U = *5 m* s^{-1}*; (b) variation* α, α, C_l *and* C_{dp} *with blade azimuth angle* (ϕ) *at* U = *10 m* s^{-1}*; and (c) variation* α, α, C_l *and* C_{dp} *with blade azimuth angle* (ϕ) *at* U = *15 m* s^{-1}

DOI: 10.1002/we

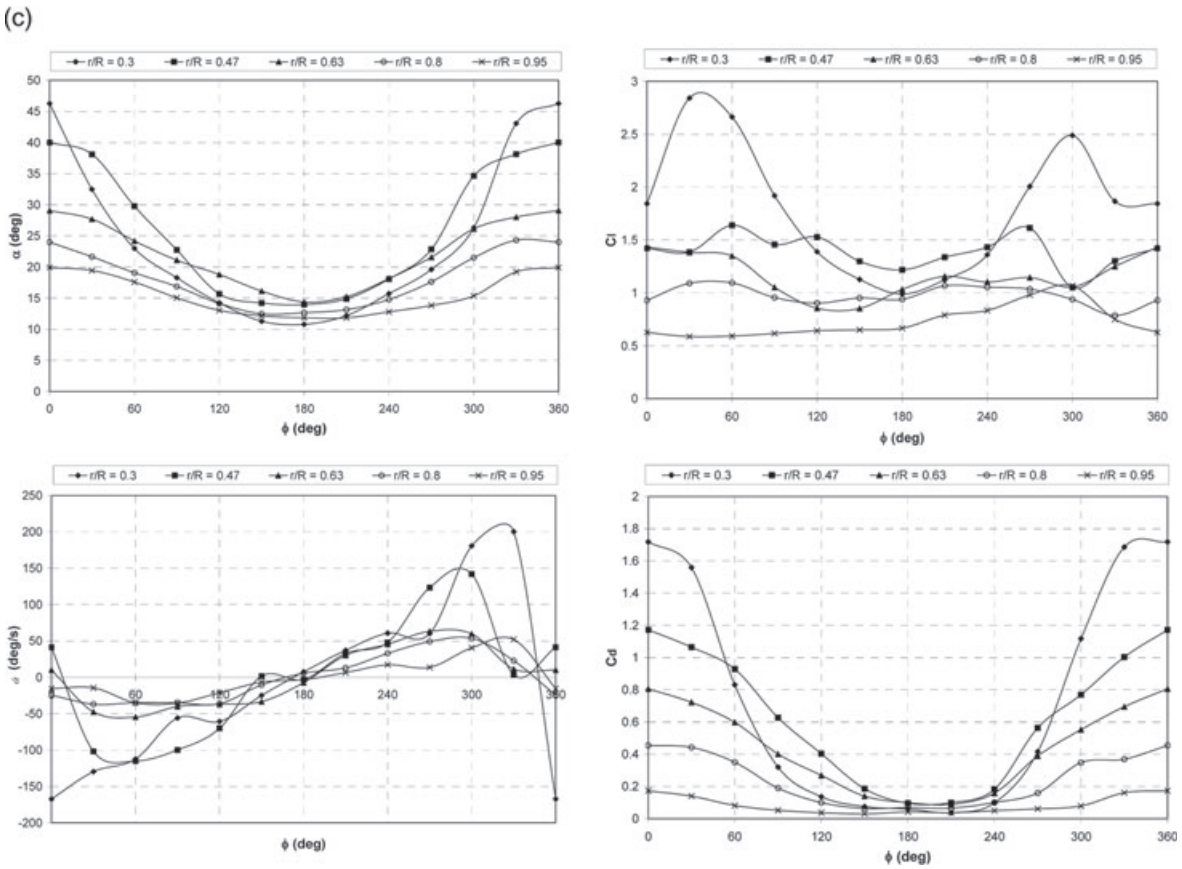

Figure 8. Continued

in mind that in a yawed rotor, these loops are not only because of cyclic angle of attack variations, but also because of a cyclic variation of the flow velocity relative to the blades. In each of these hysteresis plots, the reduced frequency k is included; k is a parameter characterizing the degree of unsteadiness at which an aerofoil is operating. The reduced frequency is given by the equation

$$k = \frac{\Omega_c}{2V_r} \tag{4}$$

where V_r is the relative flow velocity at the aerofoil. When $k = 0$, the flow is steady. When $0 < k < 0.05$, the unsteadiness in the flow is minimal and the flow may be assumed to be quasi-steady. Higher values of k are considered unsteady. Values of k equal to 0.2 and above are considered highly unsteady.

At $U = 5$ m s^{-1} (Figure 9(a),(b)), the angles of attack are small at all radial locations. Consequently, the flow over the blades is expected to be fully attached throughout the whole blade revolution. Both the lift and drag hysteresis loops are considerably wide at inboard sections ($r/R = 0.3$, 0.47), which implies that unsteady effects here are significant even though no stall is present. At the other radial locations ($r/R = 0.63$, 0.8 and 0.95), the loops are very narrow, and thus, unsteady effects here are negligible. At higher wind speeds (U = 10 and 15 m s^{-1}), the calculated angle of attack becomes very large, resulting in dynamic stall. It may be observed that much larger phase variations in C_l and C_{dp} are present than for attached flow conditions ($U = 5$ m s^{-1}). This is a result of significant hysteresis in the flow structures. The values of C_l and C_{dp} at the same angle of

DOI: 10.1002/we

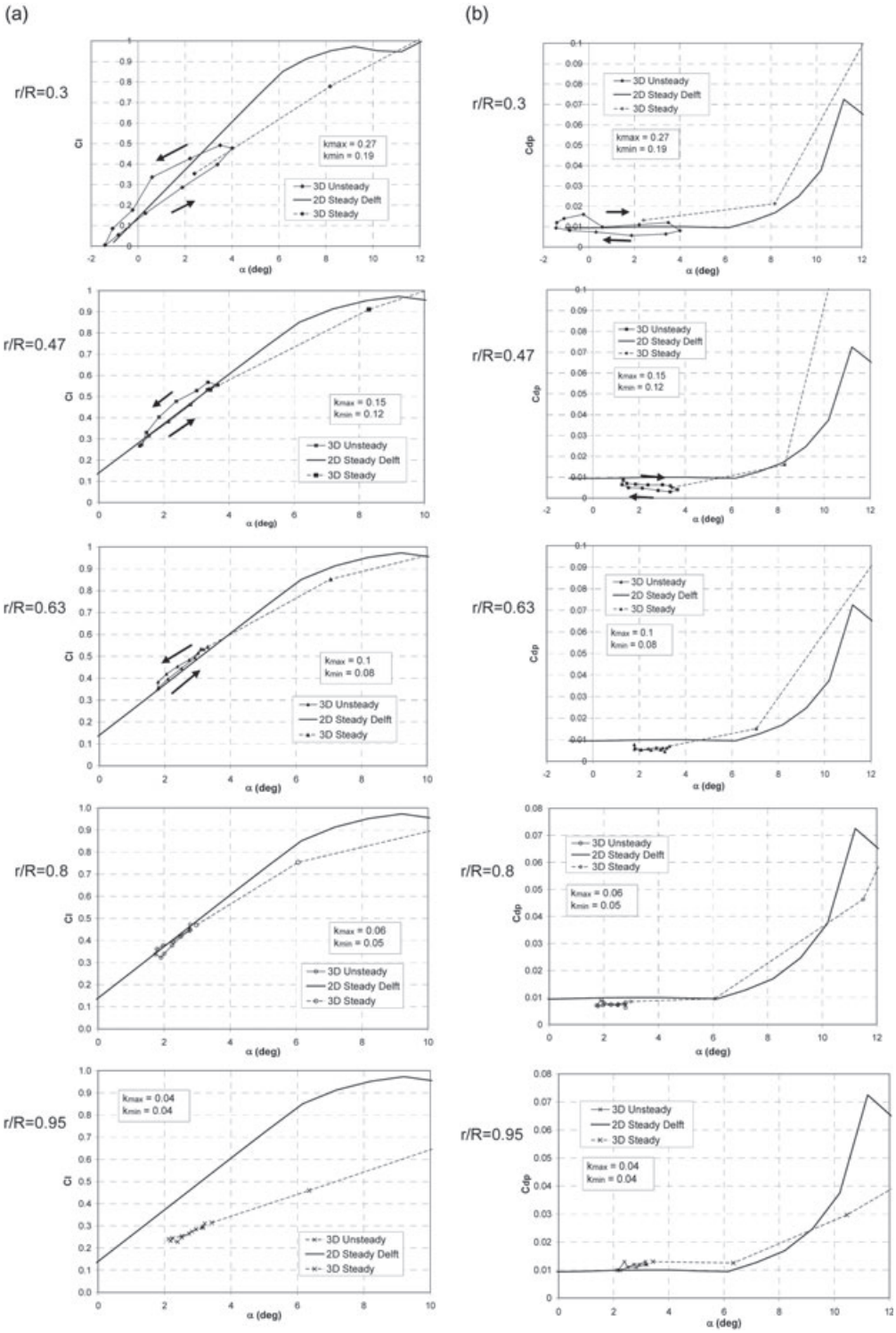

Figure 9. (a) C_l-α *hysterisis loops at* U = *5 m s*$^{-1}$*; (b)* C_{dp}-α *hysterisis loops at* U = *5 m s*$^{-1}$*; (c)* C_l-α *hysterisis loops at* U = *10 m s*$^{-1}$*; (d)* C_{dp}-α *hysterisis loops at* U = *10 m s*$^{-1}$*; (e)* C_l-α *hysterisis loops at* U = *15 m s*$^{-1}$*; and (f)* C_{dp}-α *hysterisis loops at* U = *15 m s*$^{-1}$

DOI: 10.1002/we

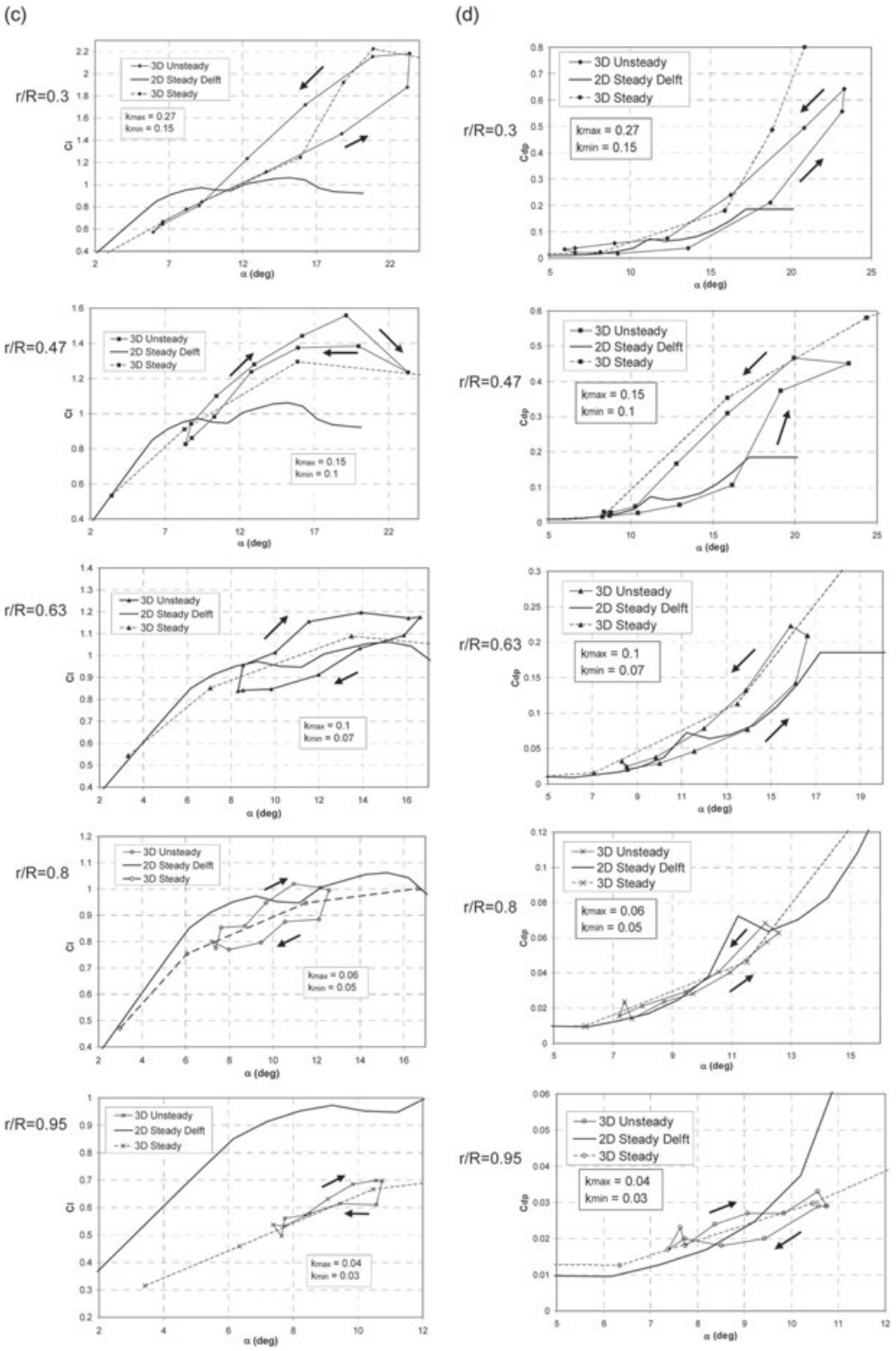

Figure 9. Continued

DOI: 10.1002/we

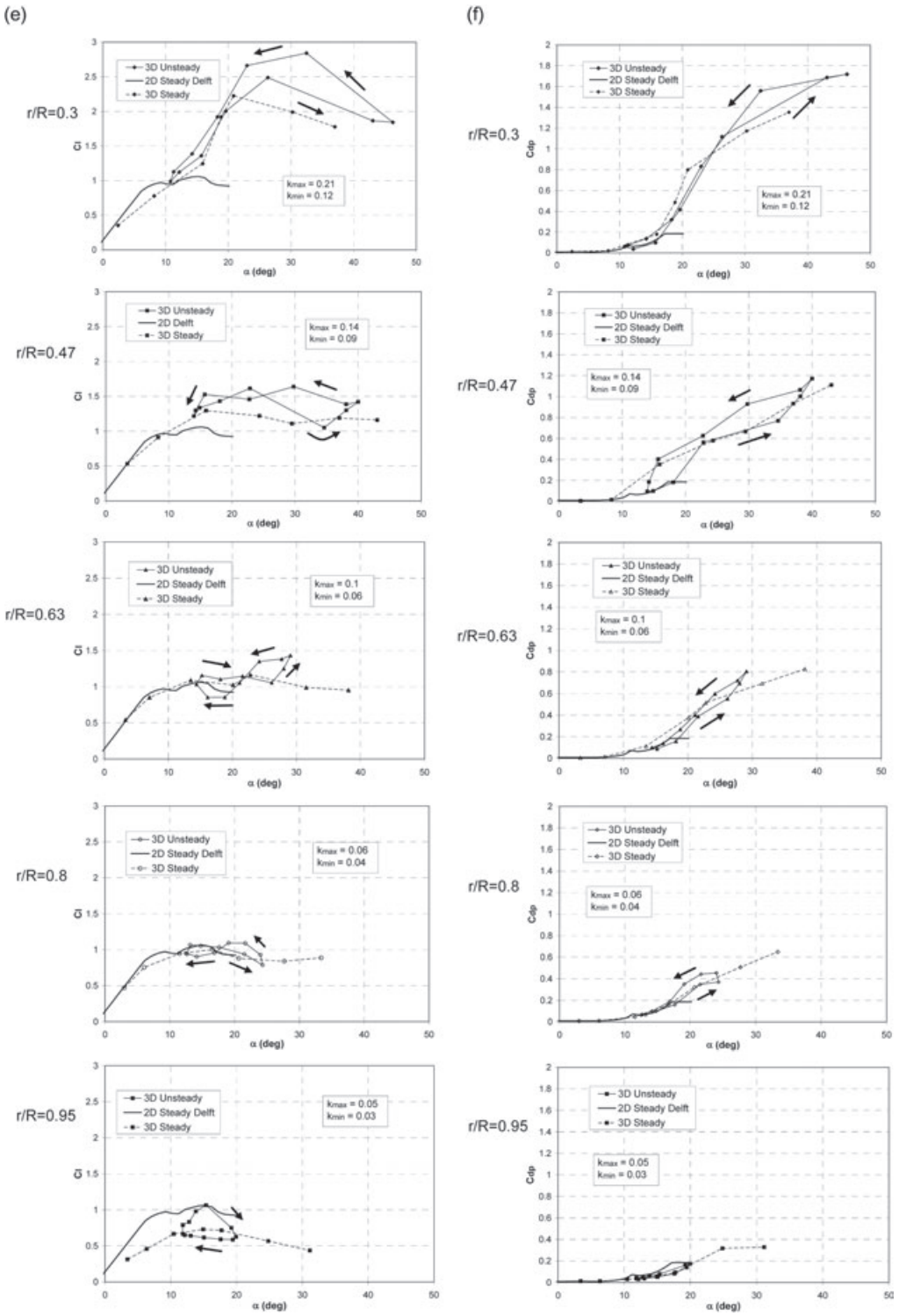

Figure 9. Continued

DOI: 10.1002/we

attack will vary on whether the flow is separating or re-attaching. In some severe cases, however, flow re-attachment may not take place since the minimum angle of attack will be too high. Figure 9(c)–(f) indicates that dynamic stall is most severe at the inboard blade sections. One may observe that the unsteady lift and drag coefficients may well exceed not only the 2-D steady values, but also the 3-D steady values derived for non-yawed conditions.

Some important comments concerning the derived hysteresis loops are:

- At each wind speed, the hysteresis loops for both C_l and C_{dp} are larger at the inboard blade sections, and unsteady effects are less pronounced at the outboard regions. However, severe unsteady effects may still take place at the blade tip, especially at high angles of attack (refer to Figure 9(e) for $r/R = 0.95$).
- In general, both the C_l and C_{dp} hysteresis loops are closer to the 3-D steady values than to the corresponding 2-D steady data. This is observed at both attached and stall conditions, and it implies that 3-D effects have a significant role in unsteady flow behaviour of wind turbine blades, in particular stall delay. This implies that a correction for 3-D effects is also necessary when correcting 2-D static aerofoil data for unsteady aerodynamic conditions.
- The hysterisis loops often change direction from counterclockwise to clockwise when moving outboard from $r/R = 0.3$–0.95. This is mainly observed in the lift hysterisis loops at $U = 10$ and $15\ \mathrm{m\ s^{-1}}$ (see Figure 9(c),(e)).

Figure 9 shows the obtained values for k at the different radial locations and wind speeds of the NREL rotor. Since in a yawed rotor, the relative velocity of the flow at each blade section (V_r) changes with blade azimuth angle (ϕ), the maximum and minimum values are included. The maximum and minimum values of k occur at approximate blade azimuth angles of 0º and 180º, respectively. It may be observed that the highest reduced frequencies occur at low r/R values. However, changing the wind speed does not alter the reduced frequencies at each radial position significantly. This is a consequence of the fact that the rotor angular speed is kept constant, and the wind tunnel speed is much smaller than the rotor angular speed ($U << r\Omega$).

More detailed analysis of the unsteady aerodynamic effects may be carried out by analyzing the derived hysteresis loops in conjunction with the analysis of the unsteady chordwise blade pressure distributions measured in the wind tunnel. The latter analysis is very helpful in identifying the flow characteristics on the blades at each angle of attack, as described by Schreck *et al.*[16,22]

Bound Circulation Distributions at Blades

Figure 10 illustrates 3-D plots of the bound circulation distributions at the blades as a function of radial position (r/R) and blade azimuth angle (ϕ). For the lowest wind speed ($U = 5\ \mathrm{m\ s^{-1}}$), at which the flow over the blades is considerably attached, the 3-D plot takes the shape of a saddle. At each blade azimuth angle, the peak bound circulation occurs close to the middle blade section. The peak circulation is highest at blade position equal to 0º/360º, and is lowest at about 180º. At high wind speeds, where separated flow conditions are known to occur ($U = 10, 15\ \mathrm{m\ s^{-1}}$), the saddle-shaped distribution is no longer present and a rather irregular distribution occurs. The peak bound circulation tends to shift towards the blade root region of the blade, where in fact the highest lift coefficients are noted. However, the peak bound circulation is still observed close to blade position 0º/360º.

Wake Plots

Figures 11 and 12 present the free wake plots derived from the measured aerodynamic loading on the blades at $U = 5$ and $15\ \mathrm{m\ s^{-1}}$. Colour coding is used to denote the trailing and shed vorticity in the near wake. For each wind speed, two plots are presented: one for trailing vorticity, the other for shed vorticity. The colour coding is very helpful in better understanding how the unsteady bound circulation at the blades (refer to Figure 10) eventually diffuses into the wake downstream of the rotor in the form of trailing and shed vorticity. The presence of roll-up of the vortex sheets is apparent. Since in a yawed rotor, the bound circulation is a

DOI: 10.1002/we

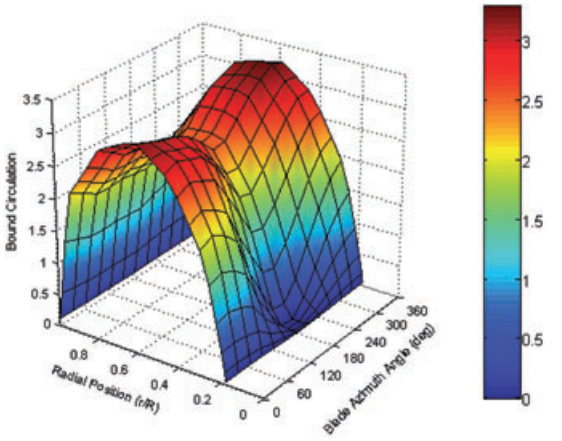

U=5m/s

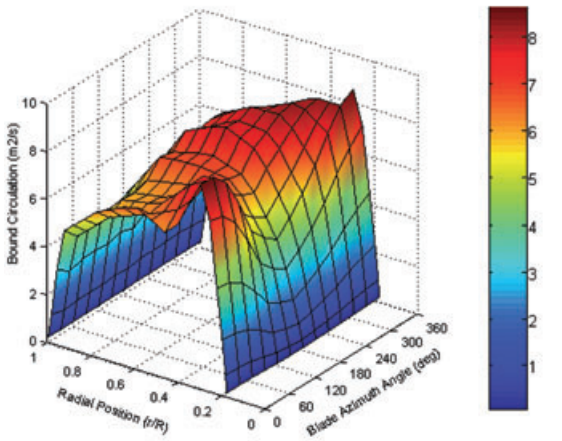

U=10m/s

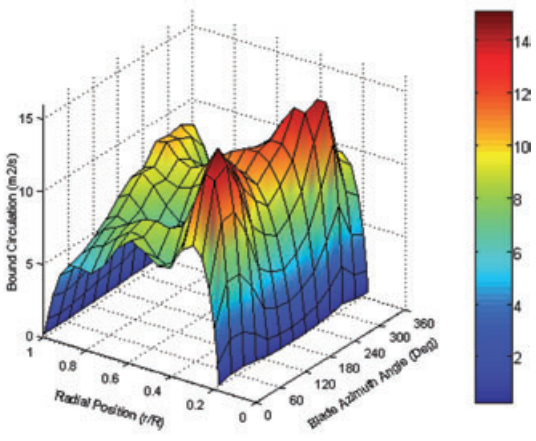

U=15m/s

Figure 10. Variation of bound circulation at blades with radial location and blade azimuth angle

DOI: 10.1002/we

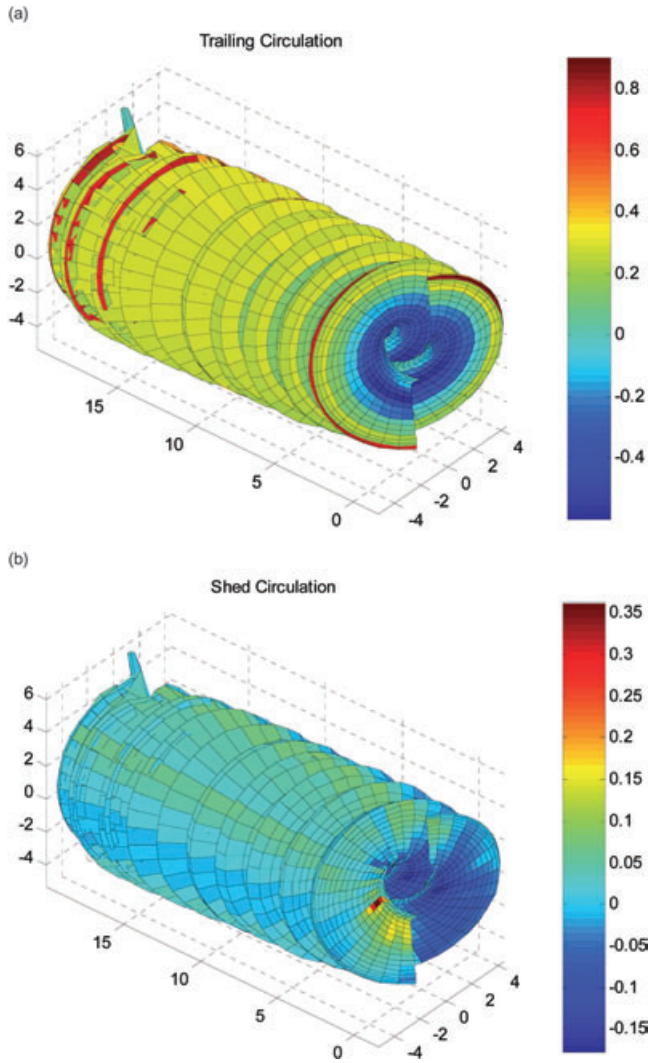

Figure 11. Free wake plots for U = 5 m s^{-1}. *Color coding (shading) denotes trailing and shed circulation distribution in wake*

function of rotor azimuth angle, the wake trailing and shed vorticity will be time dependent. Looking at Figures 11 and 12 will reveal that, at the lowest wind speed (U = 5 m s^{-1}), the trailing vorticity in the wake tends to be concentrated towards the blade tip and root regions. This is a result of the fact that the bound circulation at the blades is highest at the middle sections, but then decreases steadily to zero towards the blade tip and root (refer to Figure 10). The trailing vorticity at the tip region is positive, while it is negative at the root region. For high wind speed conditions, however, the bound circulation distribution is irregular and this yields considerable levels of 'horseshoe' trailing vorticity to be released from the middle blade sections. This is especially observed at U = 15 m s^{-1} (Figure 12(a)). Consequently, the trailing vorticity is more dispersed through the wake.

The shed vorticity levels are small at U = 5 m s^{-1} when compared with the trailing vorticity levels. At higher wind speeds (U = 10, 15 m s^{-1}), higher shed vorticity levels are observed at local spots of the wake vortex sheets. However, the shed vorticity across most of the vortex sheets remains small in magnitude in comparison with the trailing vorticity.

DOI: 10.1002/we

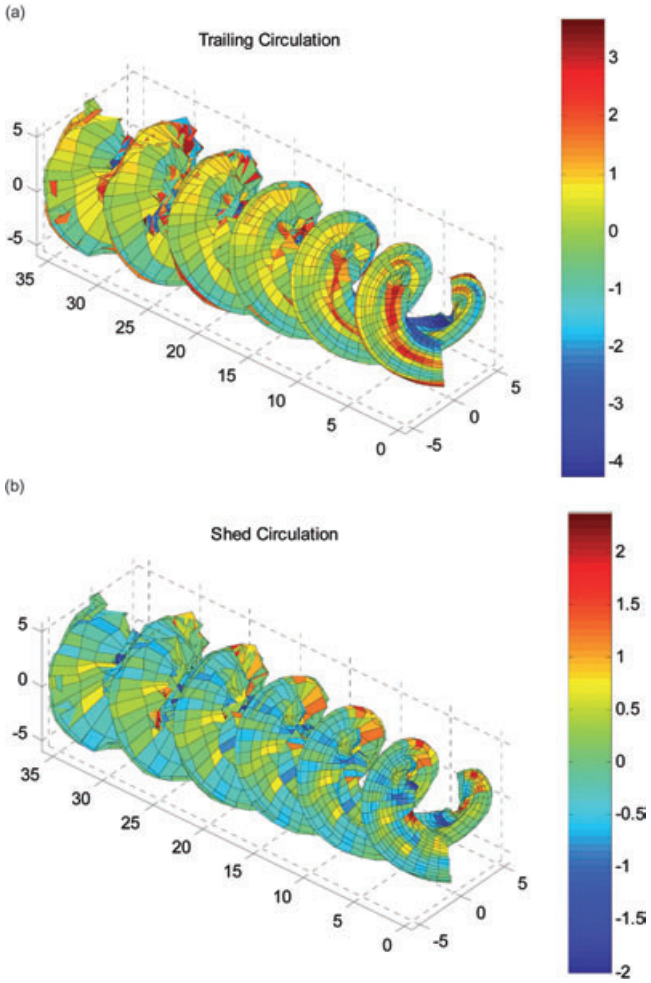

Figure 12. Free wake plots for U = *15 m s*$^{-1}$. *Color coding (shading) denotes trailing and shed circulation distribution in wake*

From the wake geometry, it is possible to derive the approximate pitch of the tip vortex pitch. In the study, this was derived by taking a cross-sectional plane through the free wake, with the plane being horizontal and passing through the rotor hub. Figure 13 illustrates the derived variation of the tip vortex pitch with the wind speed for yaw angle of 30º. Because of wake skewness resulting for rotor yaw, the tip vortex pitch on the upstream side of the wake is different from that on the downstream side. The corresponding tip vortex pitch variation for non-yawed conditions is also included in Figure 13. In both non-yawed and yawed conditions, the vortex sheet pitch increases approximately linearly with wind speed. For the yawed case, the pitch on the upstream and downstream side of the wake tend to be very close. However, it may be observed that, for all wind speeds, the rotor yaw decreases the vortex sheet pitch below that for zero yaw. From the wake geometry, it was noted that the predicted wake expansion was very small, and thus, very difficult to quantify from the free wake plots.

Induced Velocities at Rotor Plane

Figure 14 illustrates the unsteady axial induction factors at the rotor plane as predicted by the free wake model in accordance with the blade pressure measurements taken in the wind tunnel. Figure 14(a)–(c) shows the

DOI: 10.1002/we

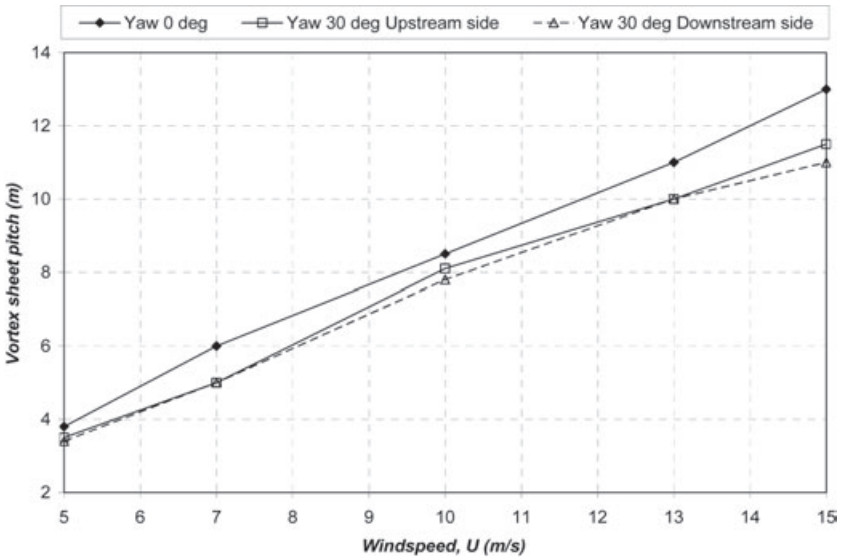

Figure 13. Variation of vortex sheet pitch with wind tunnel speed for axial condition and yaw 30 degrees

variation of the azimuthally averaged axial induction factor (i.e. annular averaged axial induction factor, a_1) at the rotor plane with rotor azimuth angle for different radial locations. Figure 14(d)–(f) shows the variation of the axial induction factor at the blade lifting line ($a_{1,c}$) with blade azimuth angle for different radial locations.

When the wind speed is low ($U = 5$ m s^{-1}), the free wake model predicts an azimuthally averaged axial induction factor that is almost constant with rotor azimuth angle. However, at higher wind speeds, a considerable cyclic variation of a_1 is observed. The cyclic component is highest at the inboard blade sections. The cyclic variation has a frequency equal to $2p$ as a consequence of the fact that the rotor has two blades.

The variation of the axial induced velocity at the blade lifting line with blade azimuth angle is periodic and regular at low wind speeds ($U = 5$ m s^{-1}), especially at the outboard regions of the blades (see Figure 14(d)), but then becomes very irregular at higher wind speeds ($U = 10$, 15 m s^{-1}; see Figure 14(e),(f)). At low wind speeds, the periodic variation of $a_{1,c}$ with ϕ has a phase angle that changes depending on the radial position (r/R) of the blade section. This is because of the fact that in a skewed wake, the proximity of the blades to the wake vorticity is a function of both blade azimuth angle and radial location. Recall from 'Wake Plots' that at the low wind speeds, the trailing vorticity in the wake tends to be concentrated at the tip and root regions. The outboard blade sections are in general closer to the wake vorticity that is originating from the blade tips at blade azimuth position of 90º than at 270º. Consequently, the induced velocity at the outboard blade sections is higher at 90º than at 270º, as in fact depicted in Figure 14(d). As one moves inboard, the proximity of the blade sections to the wake vorticity originating from the tip decreases, but this is followed by an increased proximity to the wake vorticity originating from the blade roots. This causes the maximum induced velocity to occur at a different blade azimuth angle, thus changing the phase angle of the variation of $a_{1,c}$ with $\tilde{\phi}$.

At higher wind speeds ($U = 10$ and 15 m s^{-1}), the presence of 'horseshoe' trailing vorticity levels at the middle blade sections distorts the periodic variation of $a_{1,c}$ with ϕ at all radial locations, making it very irregular.

From the results of this study, one can easily remark the following deficiencies of Glauert's equation (1) (or similar models) usually implemented in BEM-based aerodynamic codes:

- Glauert's model assumes that the azimuthally averaged axial induced velocity (a_1) does not vary with rotor azimuth angle. Although this assumption may be realistic at high tip speed ratios, it does not necessarily apply for high wind speed conditions where the flow is separated.

DOI: 10.1002/we

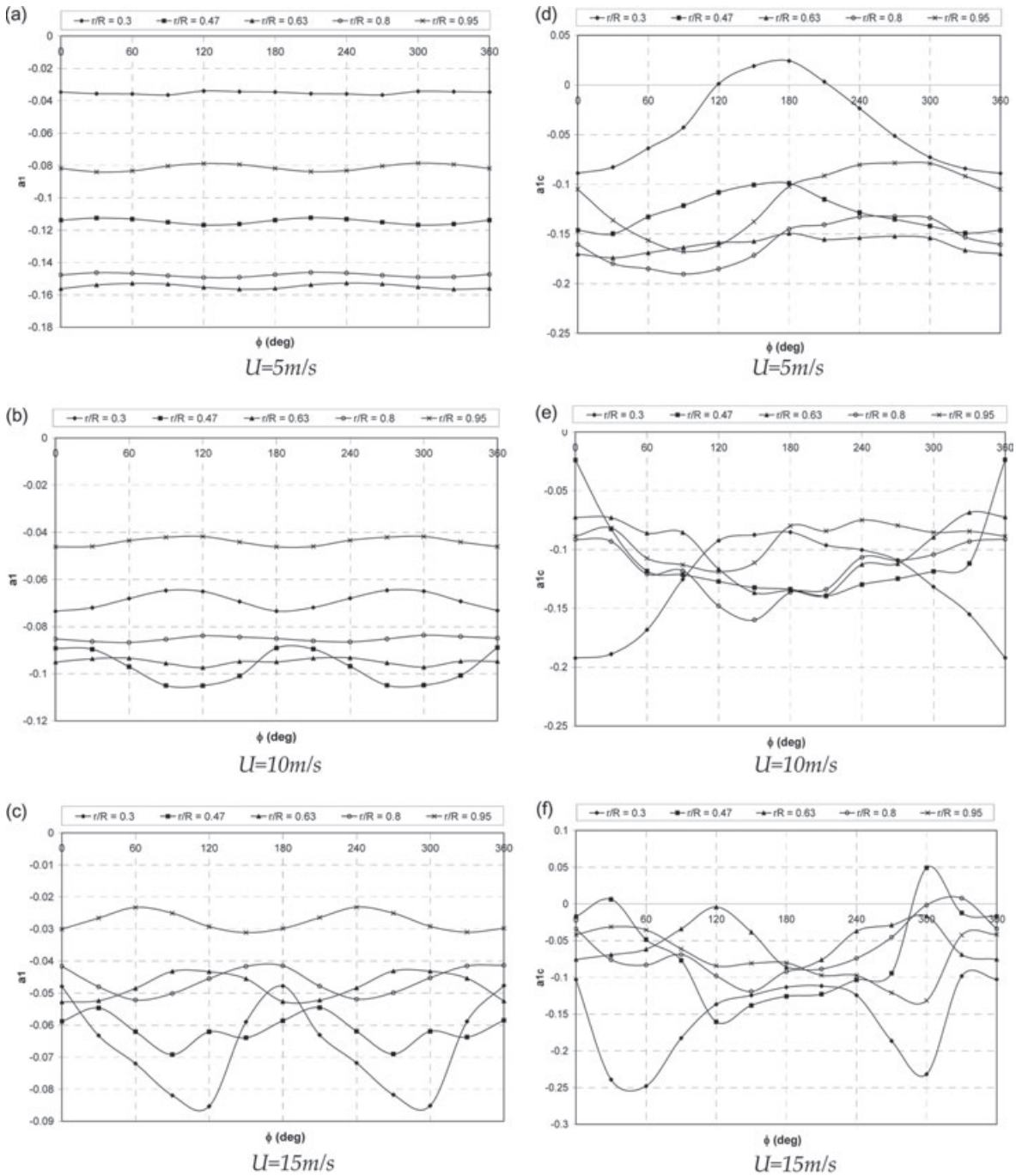

Figure 14. Variation of axial induction factors a_1 *and* $a_{1,c}$ *with blade/rotor azimuth angle (*ϕ*) at* $U = 5$, *10 and 15 m s*$^{-1}$

- Glauert's model does not cater for the phase angle change with radial location of the variation $a_{1,c}$ with ϕ, resulting from root circulation. Also as noted,[10] root circulation effects may create an induced velocity distribution that has a higher harmonic content than only 1p.
- Glauert's model is invalid for low tip speed ratios with stalled flows where the variation $a_{1,c}$ with ϕ becomes very irregular.

DOI: 10.1002/we

As already described in Results and Discussion, in the free vortex computations of this study, the induction at the lifting line of the blades is caused by the free wake trailing and shed vorticity and because of the trailing vorticity of the prescribed far wake model. The induction at the lifting line caused by bound circulation from the two blades is zero. This is a consequence of the fact that a lifting line model is used to represent the blades and also because both lifting lines are in-line with one another (no blade coning). As already mentioned in Methodology, in the free wake calculations, the near wake parameter *nRev* was selected large enough so that the induction contributed by the far wake is very small. Thus, it may be assumed that the total induction is because of trailing and shed vorticity of the near wake only. Using this free wake model, it is possible to calculate the induced velocity components resulting from the near wake trailing and shed vorticity separately. In this way, it would be possible to determine which vorticity type has the greater influence on the flow at the blades. The induced velocities of Figure 14 are shown again in Figure 15 for $U = 5$ and 15 m s^{-1}, but including the individual induced velocity components because of trailing and shed vorticity. The induced velocity by the shed vorticity is in general very small. This is observed even at $U = 10$ m s^{-1}. This proves that the trailing vorticity is by far more dominant than the shed counterpart. The induction component caused by the far wake alone is also included in Figure 15, and as it may be observed it is very small compared to the total induction.

Global Loads

The unsteady lift and drag coefficients and induced velocities derived by the free wake vortex model were used to calculate the low-speed shaft torque and the blade flap/edgewise bending moments using the blade element theory equations. These results are shown in Figure 16(a)–(c) where they are noted by plots 'free wake'. As a cross-check for these calculations, the same loads were computed directly from the experimental data by using a linear interpolation to obtain a distribution for C_n, C_t and Q_{NORM} across the whole blade span. In the linear interpolation, C_n and C_t at the blade tips were set equal to zero. The trapezium rule was adopted for integrating numerically across the whole blade span. These results are included in Figure 16 and are referred to as 'exp'. The loads measured directly using strain gauges are also included in this figure. The results calculated by the free wake model and those derived directly from the pressure measurements ('exp') agree very well. However, agreement with the loads measured by the strain gauges is not as good. The reasons for the discrepancies between the free wake results and the strain gauge measurements are various. First of all, the free wake model only calculates aerodynamic loads, and the loads caused by gravity and structural dynamics are not accounted for. Gravitational loads are not included, and thus, the computed edgewise moment does not include the cyclic component induced by the blade weight. This leads to a large discrepancy in Figure 16(c). A second important reason for the discrepancy between the free wake results and the strain gauge measurements is because of the measurement of C_t. This could be noted from the discrepancy between the azimuthally averaged values of the *LSSTQ* and *REM* obtained from the strain gauge measurements and free wake results. The discrepancy is more significant at higher wind speeds ($U = 10$ and 15 m s^{-1}) where the angles of attack are larger. The same has already been found when treating axial conditions, as documented.[24] It is well known that C_t values determined from pressure measurements are very sensitive to the capture of peak suction at the leading edge. The amount of sensors used on the subject NREL measurements was only 22, and it is probable that the peak value of suction was missed, leading to an error in the derived values of C_t. Further work is required to be able to quantify the errors in the derived aerofoil data caused by errors in the measured values of C_t.

In the free wake model, aerodynamic influences caused by the tower and rotor nacelle were not included. However, the very good agreement obtained between the loads calculated by the free wake code ('free wake') and those derived directly from the pressure measurements ('exp') might imply that these aerodynamics influences are minimal.

Comparison of α and LFA

Figure 17 compares the unsteady angle of attack variations derived from the blade pressure measurements in conjunction with the free wake vortex model with the unsteady LFA variations measured by

DOI: 10.1002/we

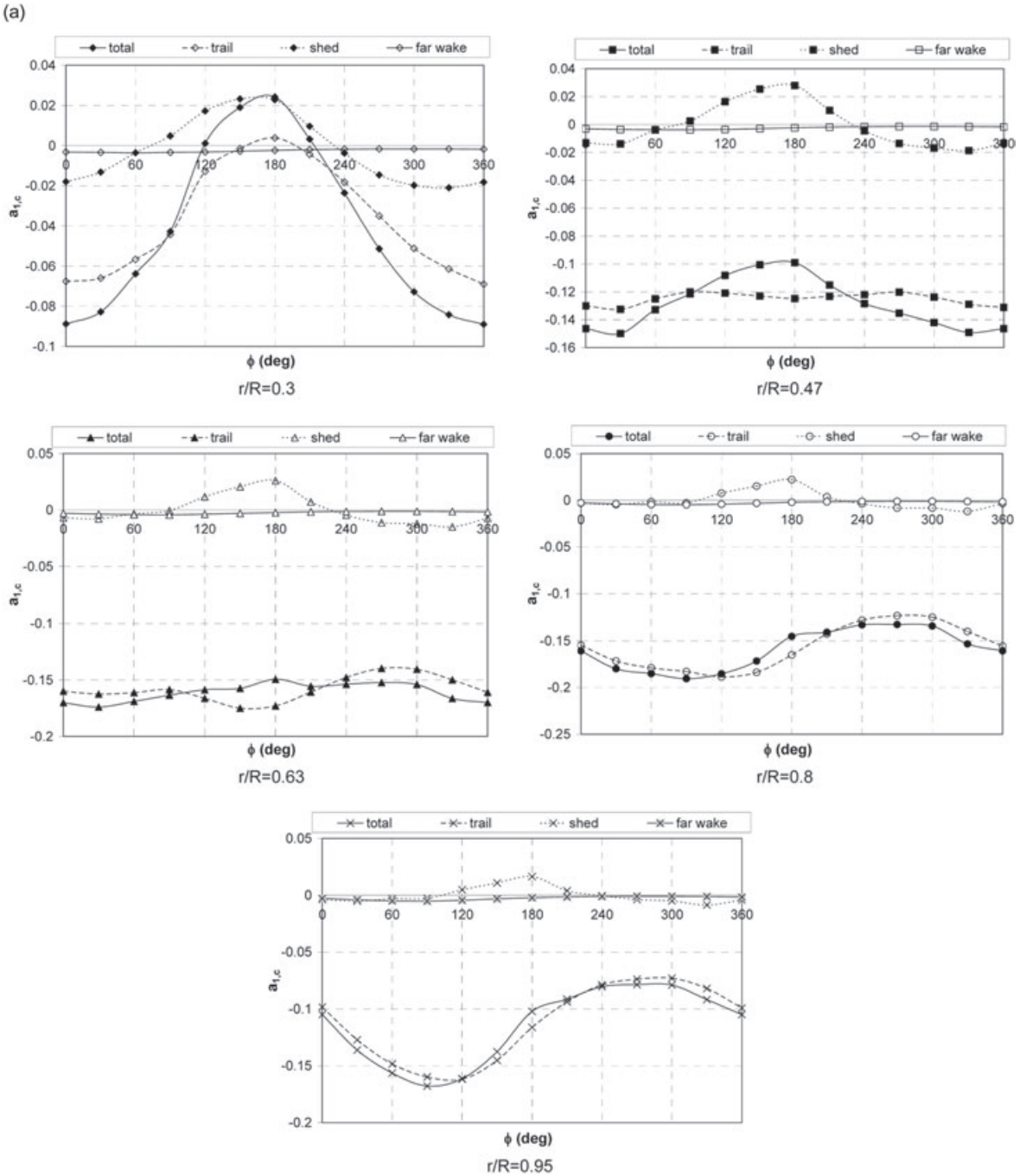

Figure 15. (a) Contribution of circulation components from near and far wake to the induction factor at blade line at U = *5 m s*$^{-1}$*; and (b) contribution of circulation components from near and far wake to the induction factor at blade line at* U = *15 m s*$^{-1}$

the flow direction probes at $U = 10\,\mathrm{m\,s^{-1}}$. Large differences are noted between the two parameters at all azimuth positions of the blades. These differences indicate the necessity for some form of correction when deriving the angle of attack directly from the measured LFA. However, one should also keep in mind that the probe was subjected to highly unsteady flow situations. At $U = 10\,\mathrm{m\,s^{-1}}$,

DOI: 10.1002/we

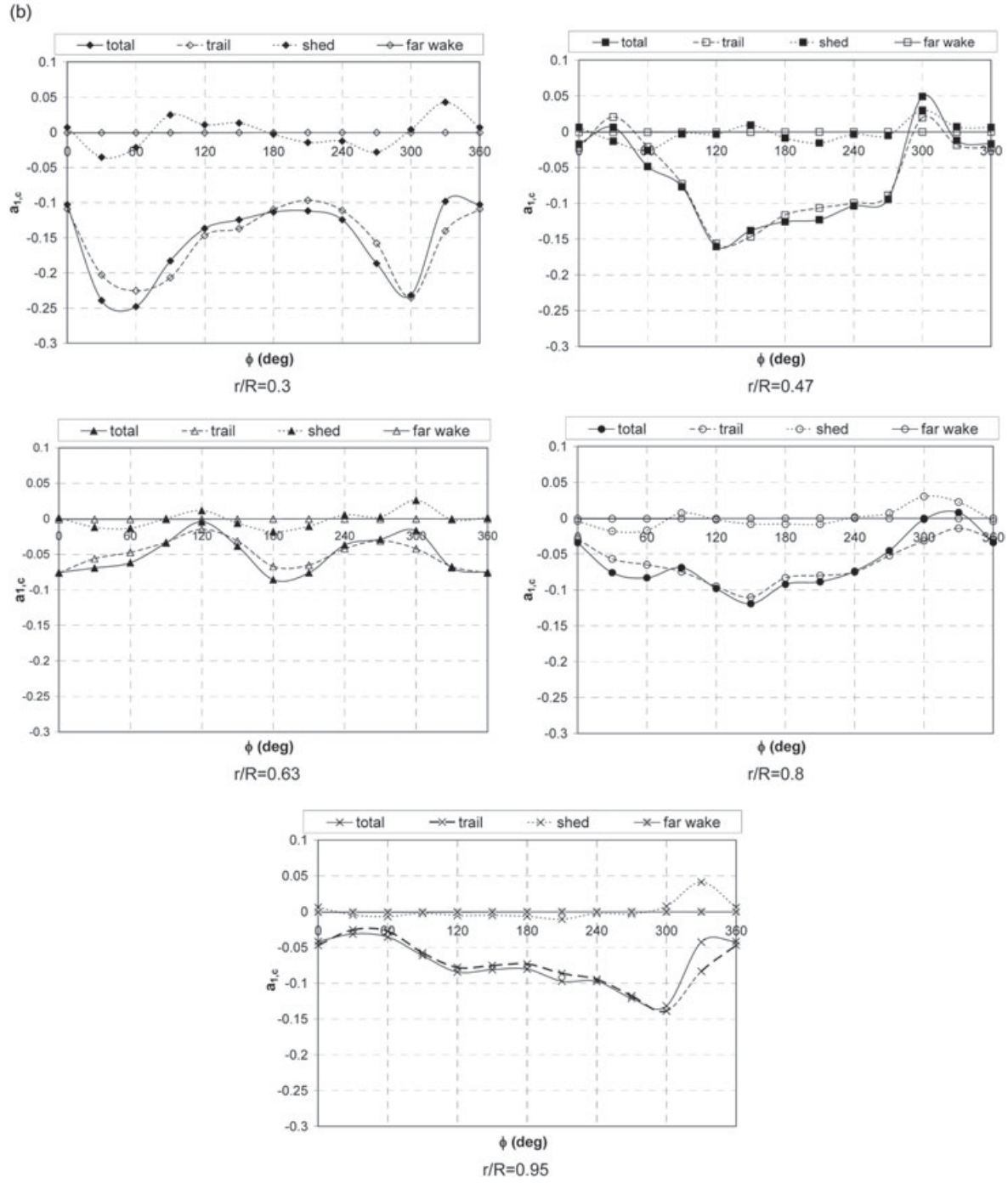

Figure 15. Continued

the free wake model estimates that the time rate of change of angle of attack reaches a peak of about ±78 deg s^{-1} (refer to Figure 8(b)) at the inboard sections. Further work is required to establish the accuracy with which five-hole pressure probes manage to measure the LFA at such high levels of unsteadiness.

DOI: 10.1002/we

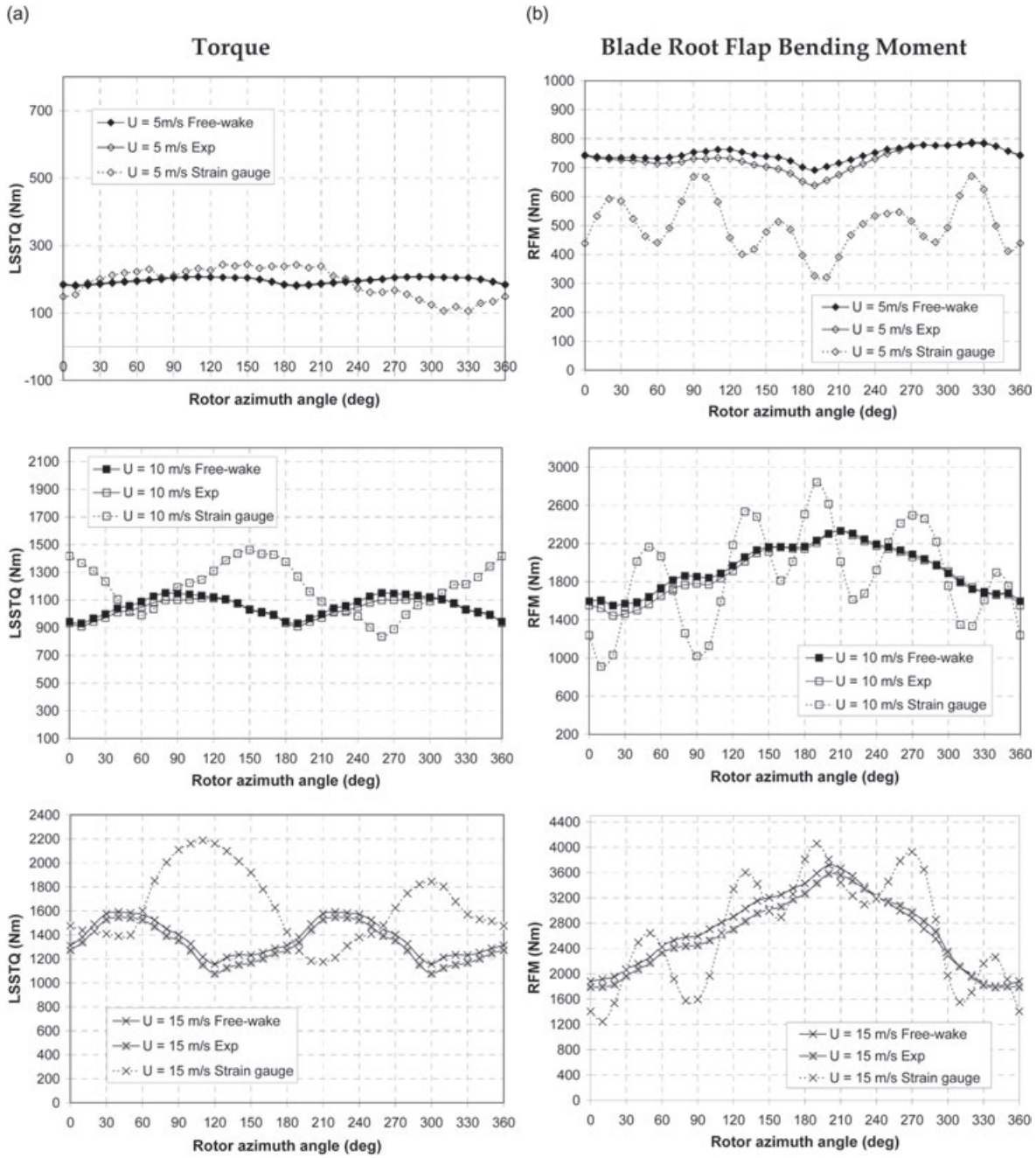

Figure 16. (a) Variation of low-speed shaft torque with rotor azimuth angle (ϕ) at U = *5, 10 and 15 m s*$^{-1}$*; and (b) variation of blade root flap bending moment with rotor azimuth angle (ϕ) at* U = *5, 10 and 15 m s*$^{-1}$

Conclusions

This paper describes a method in which a free wake vortex model is used in conjunction with the blade pressure measurements to investigate the aerodynamic behaviour of a wind turbine in yaw. It is shown that, using a free wake vortex model, it is possible to derive the unsteady angle of attack distributions from knowledge of the aerodynamic normal and tangential forces acting on the blades of a yawed rotor. These distributions

DOI: 10.1002/we

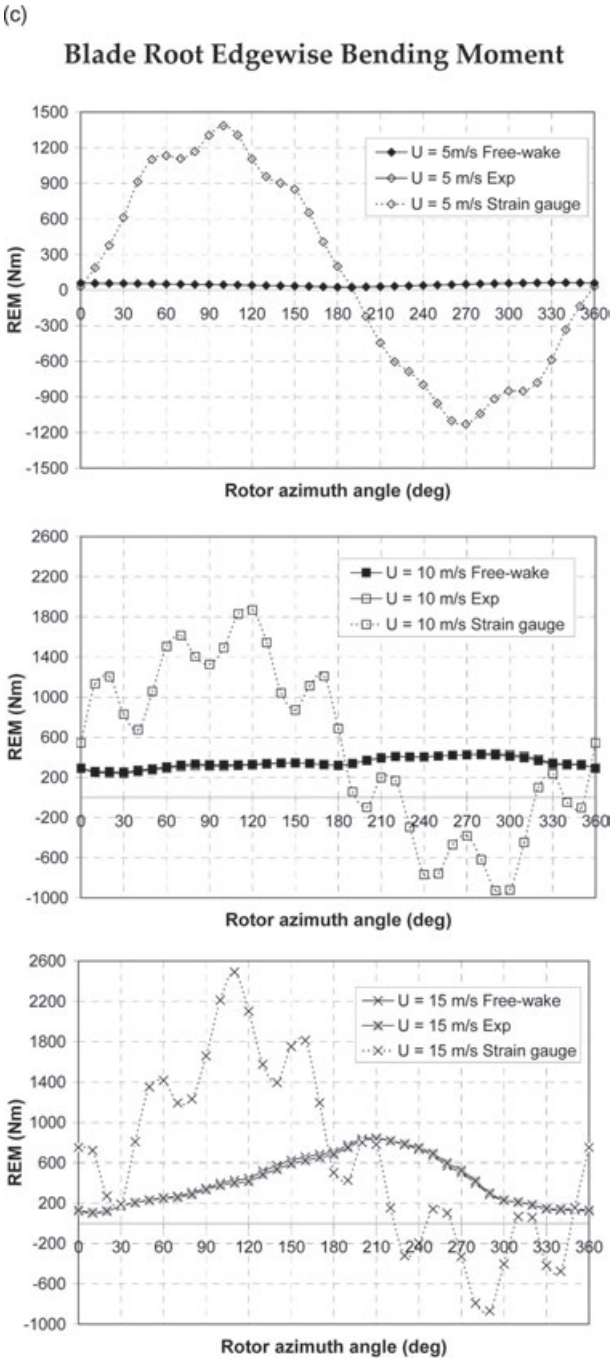

Figure 16. Continued

are used to estimate the 3-D unsteady lift and drag coefficients. At the low wind speed of $U = 5$ m s^{-1}, it is found that in the periodic variation of the angle of attack with the blade azimuth angle, there is a phase shift when moving from the inboard to outboard locations of the blades. At the higher wind speeds, however ($U = 10$ and 15 m s^{-1}), this phase shift is no longer noticeable. The unsteady 3-D aerofoil lift and drag hyster-

DOI: 10.1002/we

esis loops are found to vary significantly both with radial position and wind speed. Also, the unsteady 3-D aerofoil coefficients exceed the corresponding 3-D values derived for non-yawed conditions. It is intended to use this newly derived unsteady aerofoil data to develop more reliable engineering models for BEM-based design codes.

With regard to the variation of the axial induced velocity at the blades with blade azimuth angle, it is observed that this variation is only regular for low wind speeds. The phase angle of this variation changes with radial position. At high wind speeds very close to (or in) stall, this variation becomes very irregular and this may impose difficulties in developing improved simple engineering models for BEM-based codes. One should recall the fact that unlike helicopters, wind turbines may be operated very close or in the stall regime to be able to maximize power extraction.

The free wake plots are plotted together with the corresponding trailing and shed vorticity distributions. These provide a pictorial explanation of how the time-dependent bound circulation formed at the blades is eventually diffused into the wake under the action of complex 3-D flows. Trailing vorticity levels are found to be in general much more dominant than shed vorticity levels at all wind speeds.

Acknowledgements

The authors would like to express their gratitude to Dr. Scott Schreck of the NREL for providing the data of the phase VI wind tunnel experiments. The authors would also like to thank Ruud van Rooij for his discussion time during the course of this work.

Appendix: Nomenclature

a	index to represent vortex age of trailing or shed vortex filament
a_1	azimuthally averaged axial induction factor (= u_y/U)
$a_{1,c}$	axial induction factor at blade lifting line (= $u_{y,c}/U$)
c	local blade chord (m)
d	rotor diameter (m)
i	blade station number or trailing vortex filament number
$nRev$	number of rotor revolutions to generate near free wake
r	radial location of a blade section (m)
t	time (s)
$u_{y,c}$	axial induced velocity at blade lifting line (m s^{-1})
A	rotor cross-sectional area (m^2)
C_n	measured normal coefficient
C_t	measured tangential coefficient
C_l	derived lift coefficient
C_{dp}	derived pressure drag coefficient
LFA	local flow angle (deg)
LSSTQ	low-speed shaft torque (Nm)
P	measured shaft power (W)
Q_{NORM}	measured dynamic pressure (Pa)
R	rotor tip radius (m)
REM	blade root edgewise bending moment (Nm)
RFM	blade root flap bending moment (Nm)
S_c	viscous core model constant (s)
T	measured axial thrust (N)
U	wind tunnel speed (m s^{-1})
V_n	normal component of flow velocity relative to blade section (m s^{-1})
V_r	flow velocity relative to blade section (m s^{-1})

DOI: 10.1002/we

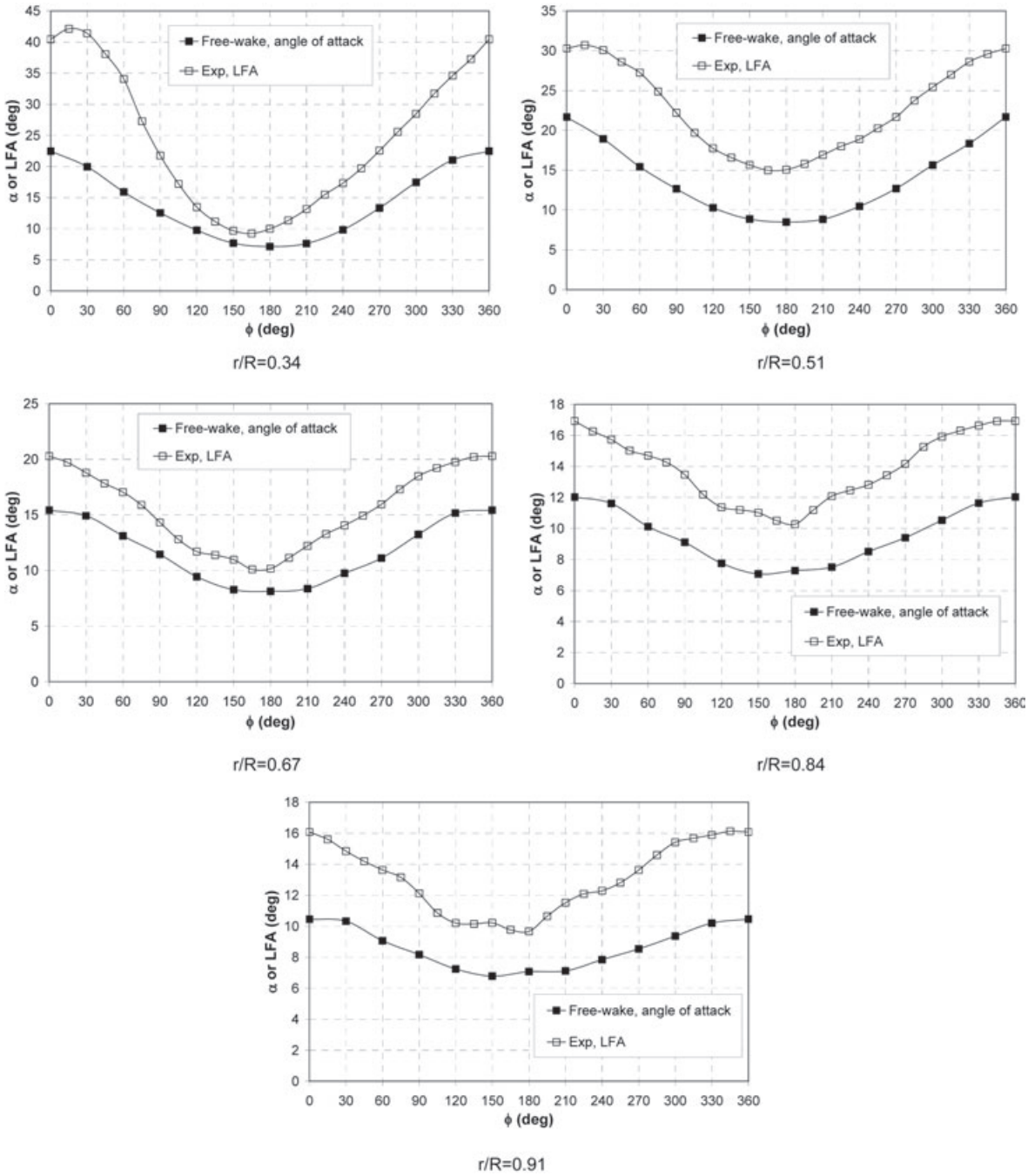

Figure 17. Variation of α *and local flow angle (LFA) with blade azimuth angle (*ϕ*) at* U = *10 m s*$^{-1}$

V_t tangential component of flow velocity relative to blade section (m s^{-1})

X-Y-Z set of co-ordinates in 3-D space with *Z* pointing vertically upwards and *Y* aligned with the direction of wind flow

Xa-Ya-Za set of co-ordinates in 3-D space with *Za* pointing vertically upwards and *Ya* aligned with the rotor shaft

DOI: 10.1002/we

α	angle of attack (deg)
$\dot{\alpha}$	rate of change of angle of attack with time (deg s^{-1})
δ_v	viscous core diffusivity coefficient
ϕ	rotor azimuth angle (equal to 0º when first blade is vertical pointing upwards) (deg)
ρ	air density (kg m^{-3})
Γ_{bound}	bound circulation (m^2 s^{-1})
Γ_{trail}	trailing vorticity (m^2 s^{-1})
Γ_{shed}	shed vorticity (m^2 s^{-1})

References

1. Snel H, Houwink R, Bosschers J. Sectional prediction of lift coefficients on rotating wind turbine blades in stall. *ECN-C-93-052*, 1993.
2. Du Z, Selig M. A 3D stall-delay model for horizontal axis wind turbine performance predictions. *AIAA-98-0021*, *ASME Wind Energy Symposium*, Reno, 1998.
3. Chaviaropoulos PK, Hansen MOL. Investigating three-dimensional and rotational effects on wind turbine blades by means of a quasi-3D Navier–Stokes solver. *Journal of Fluids Engineering* 2000; **122**: 330–336.
4. Theodorsen T. General theory of aerodynamic instability and the mechanism of flutter. *NACA Report 496*, 1935.
5. Leishman JG. *Principles of Helicopter Aerodynamics*. Cambridge University Press: Cambridge, 2000.
6. Leishman JG. Challenges in modelling the unsteady aerodynamics of wind turbines. *Wind Energy* 2002; **5**: 85–132.
7. Leishman JG. Modelling sweep effects on dynamic stall. *Journal of the American Helicopter Society* 1989; **34**: 18–29.
8. Glauert H. A general theory for the autogiro. *ARC R & M* 786, 1926.
9. Vermeer LJ. Wind tunnel experiments on a rotor model in yaw. *Proceedings of the 12th Symposium on Aerodynamics of Wind Turbines*, Lyngby, 1998; 11–20.
10. Schepers JG. An engineering model for yawed conditions, developed on the basis of wind tunnel measurements. *AIAA-99-0039 ASME Conference*, Reno, 1999.
11. Snel H, Schepers JG. (eds). Joint investigation of dynamic inflow effects and implementation of an engineering method. *ECN-C-94-107*, Netherlands Energy Research Foundation, 1994.
12. Snel H, Schepers JG. (eds). Dynamic inflow: yawed conditions and partial span pitch control. *ECN-C-95-056*, Netherlands Energy Research Foundation, 1995.
13. Schreck S. The NREL full-scale wind tunnel experiment—introduction to the special issue. *Wind Energy* 2002; **5**: 77–84.
14. Simms D, Schreck S, Hand M, Fingersh LJ. NREL unsteady aerodynamics experiment in the NASA–Ames wind tunnel: a comparison of predictions to measurements. *NREL Technical Report NREL/TP-500-29494*, 2001.
15. Tangler JL. The neboulous art of using wind tunnel aerofoil data for predicting rotor performance. *Wind Energy* 2002; **5**: 245–257.
16. Schreck S, Robinson M. Structures and interactions underlying rotational augmentation of blade aerodynamic response. *AIAA-2003-0520, Proceedings from 22nd ASME Wind Energy Symposium*, Reno, 2002.
17. Schmitz S, Chattot JJ. Application of a 'parallelized coupled Navier–Stokes/vortex-panel solver' to the NREL phase VI rotor. *AIAA-2005-0593, Proceedings from 24th ASME Wind Energy Symposium*, Reno, 2005.
18. Søresen NN, Michelsen JA, Schreck S. Navier–Stokes predictions of the NREL phase VI rotor in the NASA 80 ft × 120 ft wind tunnel. *Wind Energy* 2002; **5**: 151–169.
19. Lindenburg C. Investigation into rotor aerodynamics—analysis of the stationary measurements on the UAE phase VI rotor in the NASA–Ames wind tunnel. *ECN Report ECN-C-03-025*, 2003.
20. Laino DJ, Hansen AC, Minnema JE. Validation of the aerodyn subroutines using NREL unsteady aerodynamics experiment data. *Wind Energy* 2002; **5**: 227–244.
21. Coton FN, Wang T, McD Galraith RA. An examination of key aerodynamic modelling issues raised by the NREL blind comparison. *Wind Energy* 2002; **5**: 199–212.
22. Schreck S, Robinson M, Hand M, Simms D. Blade dynamic stall vortex kinematics for a horizontal axis wind turbine in yawed conditions. *ASME Journal of Solar Energy Engineering* 2001; **123**: 272–281.
23. Tongchitpakdee C, Benjanirat S, Sankar LN. Numerical simulation of the aerodynamics of horizontal wind turbines under yawed flow conditions. *AIAA-2005-0773, Proceedings from 24th ASME Wind Energy Symposium*, Reno, 2005.
24. Sant T, van Kuik G, van Bussel GJW. Estimating the angle of attack from blade pressure measurements on the NREL phase VI rotor using a free-wake vortex model: axial conditions. *Wind Energy* 2006; **9**: 549–577.

DOI: 10.1002/we

25. Giguere P, Selig MS. Design of a tapered and twisted blade for the NREL combined experiment rotor. *NREL/SR-500-26173*, 1999.
26. Hand MM, Simms Fingersh LJ, Jager DW, Cortell JR, Schreck S, Larwood SM. Unsteady aerodynamics experiments phase VI: wind tunnel test configurations and available data campaigns. *NREL Technical Report* NREL/TP-500–29955, 2001.
27. Leishman JG, Bhagwat MJ, Bagai A. Free-vortex filament methods for the analysis of helicopter rotor wakes. *Journal of Aircraft* 2002; **39**: 759–775.
28. Sant T. Improving BEM-based aerodynamic models in wind turbine design codes. PhD Thesis, Delft University of Technology, 2007.

DOI: 10.1002/we